Opto-Electronic Science

ISSN 2097-0382 CN 51-1800/O4

Active tuning of anisotropic phonon polaritons in natural van der Waals crystals with negative permittivity substrates and its application in energy transport

Shuo Chen, Xiaohu Wu and Ceji Fu

Citation: Chen S, Wu XH, Fu CJ. Active tuning of anisotropic phonon polaritons in natural van der Waals crystals with negative permittivity substrates and its application in energy transport. *Opto-Electron Sci* **3**, 240002 (2024).

https://doi.org/10.29026/oes.2024.240002

Received: 14 January 2024; Accepted: 4 March 2024; Published online: 6 June 2024

Related articles

Polariton lasing in Mie-resonant perovskite nanocavity

Mikhail A. Masharin, Daria Khmelevskaia, Valeriy I. Kondratiev, Daria I. Markina, Anton D. Utyushev, Dmitriy M. Dolgintsev, Alexey D. Dmitriev, Vanik A. Shahnazaryan, Anatoly P. Pushkarev, Furkan Isik, Ivan V. Iorsh, et al

Opto-Electronic Advances 2024 **7**, 230148 doi: 10.29026/oea.2024.230148

Exciton-polariton based WS_2 polarization modulator controlled by optical Stark beam

Mahnoor Shahzadi, Chuyuan Zheng, Sheraz Ahmad, Shanshan Wang, Weili Zhang

Opto-Electronic Advances 2022 **5**, 200066 doi: 10.29026/oea.2022.200066

Graphene photodetector employing double slot structure with enhanced responsivity and large bandwidth

Siqi Yan, Yan Zuo, Sanshui Xiao, Leif Katsuo Oxenløwe, Yunhong Ding

Opto-Electronic Advances 2022 **5**, 210159 doi: 10.29026/oea.2022.210159

Dual bound states in the continuum enhanced second harmonic generation with transition metal dichalcogenides monolayer

Peilong Hong, Lei Xu, Mohsen Rahmani

Opto-Electronic Advances 2022 **5**, 200097 doi: 10.29026/oea.2022.200097

More related article in Opto-Electronic Journals Group website

OES Opto-Electronic Science

http://www.oejournal.org/oes

OE_Journal

Website

Opto-Electronic Science

Article

June 2024, Vol. 3, No. 6

DOI: 10.29026/oes.2024.240002

Active tuning of anisotropic phonon polaritons in natural van der Waals crystals with negative permittivity substrates and its application in energy transport

Shuo Chen[1,2], Xiaohu Wu[2]* and Ceji Fu[1]*

Phonon polaritons (PhPs) exhibit directional in-plane propagation and ultralow losses in van der Waals (vdW) crystals, offering new possibilities for controlling the flow of light at the nanoscale. However, these PhPs, including their directional propagation, are inherently determined by the anisotropic crystal structure of the host materials. Although in-plane anisotropic PhPs can be manipulated by twisting engineering, such as twisting individual vdW slabs, dynamically adjusting their propagation presents a significant challenge. The limited application of the twisted bilayer structure in bare films further restricts its usage. In this study, we present a technique in which anisotropic PhPs supported by bare biaxial vdW slabs can be actively tuned by modifying their local dielectric environment. Excitingly, we predict that the iso-frequency contour of PhPs can be reoriented to enable propagation along forbidden directions when the crystal is placed on a substrate with a moderate negative permittivity. Besides, we systematically investigate the impact of polaritonic coupling on near-field radiative heat transfer (NFRHT) between heterostructures integrated with different substrates that have negative permittivity. Our main findings reveal that through the analysis of dispersion contour and photon transmission coefficient, the excitation and reorientation of the fundamental mode facilitate increased photon tunneling, thereby enhancing heat transfer between heterostructures. Conversely, the annihilation of the fundamental mode hinders heat transfer. Furthermore, we find the enhancement or suppression of radiative energy transport depends on the relative magnitude of the slab thickness and the vacuum gap width. Finally, the effect of negative permittivity substrates on NFRHT along the [001] crystalline direction of α-MoO_3 is considered. The spectral band where the excited fundamental mode resulting from the negative permittivity substrates is shifted to the first Reststrahlen Band (RB 1) of α-MoO_3 and is widened, resulting in more significant enhancement of heat flux from RB 1. We anticipate our results will motivate new direction for dynamical tunability of the PhPs in photonic devices.

Keywords: anisotropic phonon polaritons; forbidden direction; substrate with a negative permittivity; near-field energy transport

Chen S, Wu XH, Fu CJ. Active tuning of anisotropic phonon polaritons in natural van der Waals crystals with negative permittivity substrates and its application in energy transport. *Opto-Electron Sci* **3**, 240002 (2024).

Introduction

Polaritons, coupled modes arising from the strong interactions between photons and material excitations, provide a unique way to harness and manipulate light at

[1]LTCS and Department of Mechanics and Engineering Science, College of Engineering, Peking University, Beijing 100871, China; [2]Shandong Institute of Advanced Technology, Jinan 250100, China.

*Correspondence: XH Wu, xiaohu.wu@iat.cn; CJ Fu, E-mail: cjfu@pku.edu.cn

Received: 14 January 2024; Accepted: 4 March 2024; Published online: 6 June 2024

the nanoscale[1–6]. Conventional surface plasmon polaritons (SPPs) propagating along a metal-dielectric interface have been extensively studied in terms of intrinsic electronic scattering and plasmonic loss. The low loss and ultrahigh confinement of emergent phonon polaritons (PhPs) in van der Waals (vdW) materials (e.g., hBN, α-MoO_3, V_2O_5)[7–12] show considerable promise for integrated infrared nanophotonics. In particular, polaritons in so-called hyperbolic media, namely, hyperbolic phonon polaritons (HPhPs), exhibit hyperbolic dispersion, that is, their iso-frequency surface in momentum space is hyperboloidal-like[13,14]. Consequently, HPhPs allow an enormous density of optical states at specific wavevectors and ray-like directional polariton propagation, showing remarkable potential for application in subdiffractional focusing[15,16], thermal management[17], in-plane canalization[18–20] and hyper-lensing[21,22].

Dynamical tunability of PhPs is required for integrated nanophotonics, including adjustable propagation characteristics and reconfigurable dispersion. The hyperbolic regime of PhPs is fundamentally controlled by crystal symmetry, making tailoring the polariton topology more challenging. Recently, continuous efforts have been devoted to tuning the PhPs in anisotropic vdW materials[23–40]. Artificial nanostructures, such as grating[41], slot[42], and nanohole[20] show the ability in tuning the polaritons. However, constructing these metamaterials or metasurfaces faces difficulties in processing and manufacturing. In comparison, heterostructuring and hybridizing modes with other polaritons can modify the properties of PhPs through simple structures, attracting extensive interest[23–27]. Due to the coupling effect of evanescent waves, the PhPs in the twisted bilayer system can undergo a topological transition, i.e., the polariton topology evolves from a hyperbolic shape to an elliptical one, realizing the field canalization and dispersion flatting[28–33]. The above measure mainly adopts two or multi-layer structures, restricting its application in bare films. Another approach to manipulating PhPs is to construct the graphene/polar vdW heterostructures[34–36], in which the hybrid modes with both phonon and plasmon characteristics can be actively modified by changing the chemical potential through the gating or doping method. This idea has been widely explored in the dynamic control of polaritons involving hBN and α-MoO_3. Moreover, considering that polaritons are sensitive to the local environment, the effect of substrate plays a significant role in tailoring the polaritons[37–40,43]. Image polaritons or acoustic polaritons[44,45] are investigated when hBN or α-MoO_3 are placed in proximity to a metal plate with a thin dielectric spacer. However, previous studies mainly focus on materials with large negative permittivity, like Au or positive permittivity like SiO_2, since they are commonly used in practice. The effect of substrate media with moderate negative permittivity on PhPs has so far remained elusive. In addition, a systematic analysis about the effect of the superstrate and substrate has not been explored. Thus, it is critical to quantify how the local dielectric environment of the substrate modifies propagating PhPs.

The natural anisotropic vdW materials provide an ideal platform for exploiting the effect of in-plane anisotropy in the application of planar optical devices. Especially, in the hyperbolic regime, the theoretically infinite wavevectors and extremely large optical density of states open the door to enhance and modulate the thermal radiation and heat transfer. In addition to tuning PhPs through substrate effect, it is equally important to investigate the effect of practical substrate media on the near-field radiative heat transfer (NFRHT) when considering experimental implementations. However, the fundamental studies on the substrate effect on electromagnetic energy transfer are still scarce, hindering its further exploration and applications.

Here, we present a comprehensive study of the effect of substrate with negative permittivity on the hyperbolic phonon polaritons. We theoretically demonstrate that a reorientation of the iso-frequency contour (IFC) of hyperbolic polaritons in a biaxial slab can be engineered to allow propagation along forbidden directions when the slab is laid on a substrate with a moderate negative permittivity. In addition, we reveal that the substrate with negative permittivity can generate the elliptical-like fundamental mode which is suppressed in the configuration with a substrate having positive permittivity. In particular, we demonstrate that the direction of propagation of in-plane HPhPs in an α-MoO_3 slab can be rotated by 90°, namely, along the intrinsically forbidden direction in a bare slab by placing the slab on a SiC substrate. In the heterostructure consisting of α-MoO_3 and Au, the fundamental mode with elliptical IFC is excited. Besides, we systematically study the effect of the polaritonic coupling between heterostructures integrated with different substrates on radiative heat transfer. The effect of the excitation, reorientation, and annihilation of the fundamental mode on photon tunneling is analyzed via

dispersion contour and photon transmission coefficient (PTC). The enhancive or suppressive effect depends on the relative magnitude of gap size and slab thickness. Depending on the substrates, the coupling effect can modulate the radiative heat transfer and photon tunneling. Finally, the effect of the crystalline direction on NFRHT between heterostructures integrated with the substrate of SiC and Au is also considered and compared with the suspended configuration.

Theory and model

To elaborate on the theoretical conditions upon which this reorientation of the directional propagation of HPhPs can take place, let us start analyzing the general case of an α-MoO_3 slab embedded between two semi-infinite isotropic media with dielectric functions ε_1 and ε_3 as shown in Fig. 1(a). The α-MoO_3 slab has been recently revealed as a biaxial vdW crystal with natural hyperbolicity in the mid-infrared region. The optical response of the α-MoO_3 is dominated by the phonon absorption and its permittivity tensor components can be described by a Lorentz model:

$$\varepsilon_j = \varepsilon_\infty^j \left(1 + \frac{\omega_{L,j}^2 - \omega_{T,j}^2}{\omega_{T,j}^2 - \omega^2 - \mathrm{i}\omega\Gamma_j}\right), \tag{1}$$

where $j = x, y, z$, and detailed parameters can be found in ref[9,46]. Here, the principal axis of α-MoO_3 crystal coincides with the Cartesian coordinate axis. Without rotation, the crystal axes [100], [001], and [010] correspond to the x, y, and z axes in the Cartesian coordinate system, respectively. α-MoO_3 supports phonon polaritons (PhPs) in three Reststrahlen bands (RBs): RB 1 in the range from 545 to 851 cm^{-1} and RB 2 in the range from 820 to 972 cm^{-1}, in which the in-plane iso-frequency contour is hyperbolic; while an in-plane dispersion of elliptical shape exists for PhPs in RB 3 (from 958 to 1010 cm^{-1}), as shown in Fig. 1(b). Without loss of generality, we assume the representative dielectric functions in RB 2, where $\mathrm{Re}(\varepsilon_x) < 0$, $\mathrm{Re}(\varepsilon_y) > 0$, and $\mathrm{Re}(\varepsilon_z) > 0$. The dispersion relation of polaritons in the biaxial slab in the high-momenta approximation reads[47]

$$k(\omega) = \frac{\rho}{d}\left[\arctan\left(\frac{\varepsilon_1\rho}{\varepsilon_z}\right) + \arctan\left(\frac{\varepsilon_3\rho}{\varepsilon_z}\right) + \pi l\right], \quad l = 0, 1, 2, \ldots, \tag{2}$$

where $k = \sqrt{k_x^2 + k_y^2}$ is the modulus of the in-plane wavevector component $\boldsymbol{k}$, $\rho = \mathrm{i}\sqrt{\varepsilon_z / (\varepsilon_x \cos^2\varphi + \varepsilon_y \sin^2\varphi)}$ with φ being the angle between the x axis and $\boldsymbol{k}$, as shown in Fig. 1(a), d represents the thickness of the biaxial slab and l denotes the order of different polaritonic modes, where l = 0 represents the fundamental mode, and l = 1, 2, 3 … denotes higher-order mode. Since $\arctan(x) + \arctan(y) = \arctan((x + y) / (1 - xy))$, Eq. (2) can be conveniently rewritten as:

$$\tan\left(\frac{kd}{\rho}\right) = \frac{\rho(\varepsilon_1 + \varepsilon_3)}{\varepsilon_z} \Big/ \left(1 - \frac{\rho^2\varepsilon_1\varepsilon_3}{\varepsilon_z^2}\right). \tag{3}$$

The propagation direction and the shape of the iso-frequency contour are not trivial for the general case of arbitrary complex dielectric functions. Therefore, we assume that the permittivities of the biaxial slab are purely real. This assumption is reasonable under a small loss.

In this section, we consider only the fundamental mode, i.e., l =0. Considering that the dielectric function of the substrate is negative, i.e., $\varepsilon_3 < 0$, and that of the superstrate is positive, i.e., $\varepsilon_1 > 0$, we derive the conditions under which PhPs propagate along the x or y axis in RB 2 where $\varepsilon_x < 0$, $\varepsilon_y > 0$, and $\varepsilon_z > 0$, according to Eq. (3). Firstly, let us study the propagation of polaritons along the x axis. In this case, we set φ = 0 and therefore,

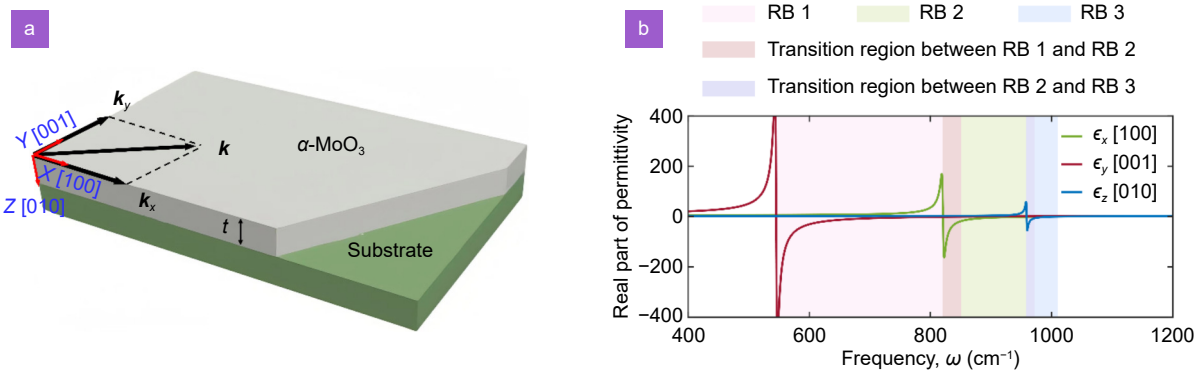

Fig. 1 | (**a**) Schematic of α-MoO_3/substrate heterostructure, where the substrate is SiC or Au. (**b**) Real parts of the components of the dielectric tensor of α-MoO_3 along the principal directions. The Reststrahlen bands are shaded in different colors.

$\rho = \mathrm{i}\sqrt{\varepsilon_z/\varepsilon_x}$. Since $\varepsilon_x < 0$ in RB 2, then $\mathrm{i}\sqrt{\varepsilon_z/\varepsilon_x} = -\sqrt{\varepsilon_z/|\varepsilon_x|}$, so Eq. (3) can be simplified as:

$$\tan\left(-\frac{kd}{\sqrt{\varepsilon_z/|\varepsilon_x|}}\right) = \frac{-\sqrt{\dfrac{\varepsilon_z}{|\varepsilon_x|}}\dfrac{(\varepsilon_1+\varepsilon_3)}{\varepsilon_z}}{1-\dfrac{\varepsilon_1\varepsilon_3}{|\varepsilon_x|\,\varepsilon_z}}, \tag{4}$$

here $0 < \dfrac{kd}{\sqrt{\varepsilon_z/|\varepsilon_x|}} < \dfrac{\pi}{2}$ due to the considered fundamental mode in this section. Consequently, the left-hand side of Eq. (4) is negative. Therefore, for Eq. (4) to have a solution, the right-hand side must also be negative. Note that $\varepsilon_1 > 0$ and $\varepsilon_3 < 0$, thus, for Eq. (4) to have a solution, the numerator on the right-hand side of Eq. (4) must be negative. Hence, we get the necessary conditions for the propagation of polaritons along x axis:

$$\varepsilon_1 + \varepsilon_3 > 0\,. \tag{5}$$

Similarly, let us study the propagation of PhPs along the y axis. In this case, we set $\varphi = \pi/2$ so that $\rho = \mathrm{i}\sqrt{\varepsilon_z/\varepsilon_y}$. Since $\varepsilon_y > 0$ in RB 2, $\sqrt{\varepsilon_z/\varepsilon_y}$ is positive and pure real. For the convenience of derivation, we set $\xi = \sqrt{\varepsilon_z/\varepsilon_y}$ (with ξ also positive and real). Thus Eq. (3) can be simplified as:

$$\tan\left(-\mathrm{i}\frac{kd}{\xi}\right) = \frac{\mathrm{i}\xi\dfrac{(\varepsilon_1+\varepsilon_3)}{\varepsilon_z}}{1+\dfrac{\varepsilon_1\varepsilon_3}{\varepsilon_z\varepsilon_y}}\,. \tag{6}$$

Taking into account that $\tan(\cdot)$ is an odd function and $\tan(\mathrm{i}\eta) = \mathrm{i}\tanh(\eta)$, Eq. (6) can be rewritten as:

$$\tanh\left(\frac{kd}{\xi}\right) = \frac{-\xi\dfrac{(\varepsilon_1+\varepsilon_3)}{\varepsilon_z}}{1+\dfrac{\varepsilon_1\varepsilon_3}{\varepsilon_z\varepsilon_y}}\,. \tag{7}$$

Note that the left-hand side of Eq. (7) is positive, so the right-hand side must also be positive. There are two cases, one is that if $\varepsilon_y\varepsilon_z + \varepsilon_1\varepsilon_3 < 0$, which holds for a high-permittivity superstrate, the necessary condition for the polaritons to propagate along the y axis reads:

$$\varepsilon_1 + \varepsilon_3 > 0\,. \tag{8}$$

The other is that if $\varepsilon_y\varepsilon_z + \varepsilon_1\varepsilon_3 > 0$ (the superstrate is a low-permittivity medium, such as air), the necessary condition becomes

$$\varepsilon_1 + \varepsilon_3 < 0\,. \tag{9}$$

Our analysis above shows that the HPhPs can propagate along the x axis when $\varepsilon_1 + \varepsilon_3 > 0$. But for PhPs to propagate along the y axis, stricter conditions should be satisfied, as listed in Table 1. Note that in the case when $\varepsilon_1 + \varepsilon_3 < 0$ and $\varepsilon_y\varepsilon_z + \varepsilon_1\varepsilon_3 < 0$ are simultaneously satisfied, the $l = 0$ mode is suppressed (i.e., annihilated).

Therefore, we demonstrate that the iso-frequency contour (IFC) of in-plane hyperbolic polaritons can realize a 90° reorientation in a biaxial slab in the neighborhood of $\mathrm{Re}(\varepsilon_1) + \mathrm{Re}(\varepsilon_3) = 0$. Namely, the HPhPs can be engineered to allow propagation along intrinsically forbidden directions by placing the slab on a substrate with a given negative permittivity. For other RBs, the fundamental mode can also be reoriented (see details in the Supplementary information). Note that for RB 3, the $l = 0$ mode cannot be excited when $\mathrm{Re}(\varepsilon_1) + \mathrm{Re}(\varepsilon_3) > 0$, while it can be excited when $\mathrm{Re}(\varepsilon_1) + \mathrm{Re}(\varepsilon_3) < 0$.

Results and discussion

We first demonstrate the reorientation of PhPs in α-MoO_3 /SiC heterostructure through the dispersion properties and electric field distributions and distinguish the type of hyperbolic polaritons based on the real and imaginary parts of the out-of-plane wavevector. Subsequently, we investigate the effect of excitation, annihilation, and reorientation of polaritons on the near-field energy transports between α-MoO_3 crystal with SiC or Au substrate in terms of the effect of vacuum gap width, the effect of thickness of α-MoO_3 slab as well as the effect of the crystalline directions of α-MoO_3.

Anisotropic polaritons along forbidden directions

To address the prediction that the propagating direction of the fundamental mode can be reoriented by changing the permittivity of the substrate, we place the biaxial

Table 1 | The relationship between the propagation direction of PhPs and the permittivities of α-MoO_3 in RB 2.

RB 2: $\varepsilon_x < 0$, $\varepsilon_y < 0$, $\varepsilon_z > 0$			
State of the fundamental mode ($l = 0$)	propagating direction of polaritons ($l = 0$)	ε_1, ε_3	Assumption ($\varepsilon_1 > 0$, $\varepsilon_3 < 0$)
Reorientation	x	$\varepsilon_1 + \varepsilon_3 > 0$	none
	y		$\varepsilon_y\varepsilon_z + \varepsilon_1\varepsilon_3 < 0$
		$\varepsilon_1 + \varepsilon_3 < 0$	$\varepsilon_y\varepsilon_z + \varepsilon_1\varepsilon_3 > 0$
Annihilation	None		$\varepsilon_y\varepsilon_z + \varepsilon_1\varepsilon_3 < 0$

vdW α-MoO_3 slab on top of the polar crystal SiC, whose relative permittivity can be described by a Lorentz model[48,49] (see details in the Supplementary information). Here, air is considered as the superstrate ($\varepsilon_1 = 1$). The permittivity of SiC (shown in Fig. S1) attains a value $\mathrm{Re}(\varepsilon_3) = -1$ at $\omega_0 = 948.6$ cm^{-1} where it approximately fulfills the critical condition $\mathrm{Re}(\varepsilon_1) + \mathrm{Re}(\varepsilon_3) = 0$. To explore the possibility, we first investigate the propagation direction of the $l = 0$ mode of the α-MoO_3 slab placed on top of SiC and compare it with the case of air substrate ($\varepsilon_3 = 1$) where the condition $\mathrm{Re}(\varepsilon_1) + \mathrm{Re}(\varepsilon_3) > 0$ is always fulfilled in the studied spectral range. Note that only if the tangential wavevector is positive, can the PhPs be excited. Therefore, to indicate the excitation of PhPs, we calculate the minimum tangential wavevector of the excited $l = 0$ mode of the α-MoO_3 slab placed on top of the SiC substrate. Taking RB 2 as an example, we get the minimum wavevector of the excited $l = 0$ mode along y-axis direction by further simplifying Eq. (7):

$$k = \frac{\xi}{d}\arctan\left(\frac{-\xi\frac{(\varepsilon_1+\varepsilon_3)}{\varepsilon_z}}{1+\frac{\varepsilon_1\varepsilon_3}{\varepsilon_y\varepsilon_z}}\right). \tag{10}$$

In RB 2, the in-plane HPhPs cannot propagate along y-axis direction for the α-MoO_3 slab embedded in air, while its direction of propagation can be rotated by 90° when the α-MoO_3 slab is placed on the SiC substrate, thus occurring along intrinsically forbidden directions. Namely, k calculated using Eq. (10) takes positive values. Note that the arctanh function parameters must be between −1 and 1 (excluding −1 and 1) due to their pure real number. Therefore, we get the spectral region (labeled as the blue shaded region) where the $l = 0$ mode propagates along the [001] direction with SiC substrate in Fig. 2(a). For other regions like the RB 1, the $l = 0$ mode propagates along the [001] direction with air substrate while along the [100] direction (forbidden direction) with the SiC substrate as shown in the blue shaded region of Fig. 2(b). Another configuration is that the substrate is replaced with Au, described with Drude and Lorentz models[50] (see details in the Supplementary information), which exhibits largely negative permittivity in the considered spectral region. As shown in Fig. S2, in the range from 958.59 cm^{-1} to 1004.68 cm^{-1}, the minimum wavevector along the [001] direction is positive, yielding a 90° rotation of the propagation direction of

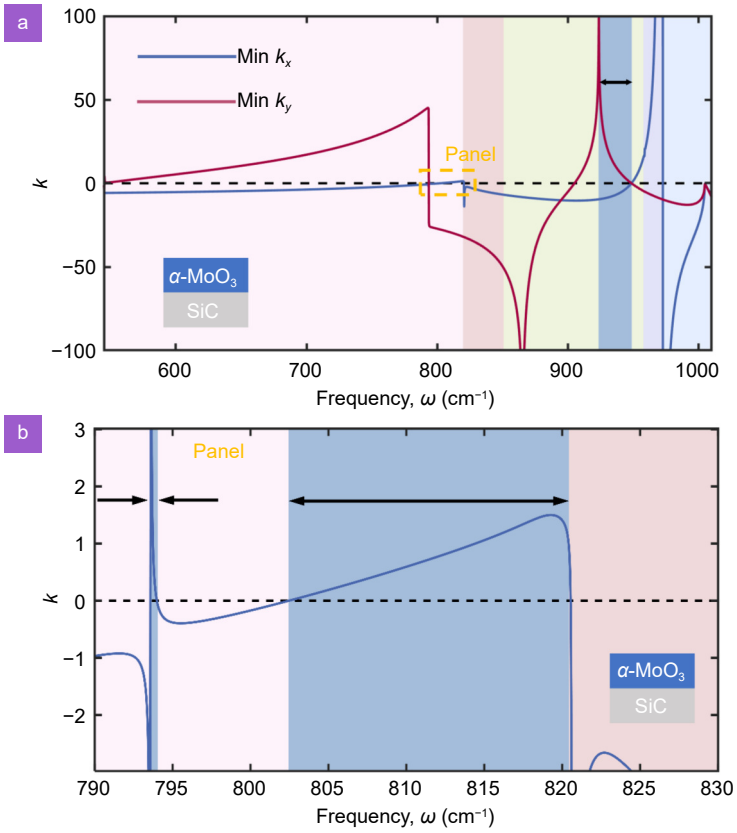

Fig. 2 | (**a**) The minimum of k_x and k_y calculated by Eq. (10). The blue shaded regions and black arrows denote the reorientation of the IFC of PhPs. (**b**) The local enlargement of the region is marked by the yellow panel in (a). The thickness of the α-MoO_3 slab is 100 nm.

HPhPs in the transition region between RB 2 and RB 3. In addition, the positive value of the wavevector in RB 3 exhibits the excitation of l = 0 mode in the α-MoO_3/Au heterostructure (See details in the Supplementary Information). However, for the other spectral regions, the excitation of l = 0 mode is suppressed.

From Eq. (10), the wavevector of l = 0 mode evidently depends on the permittivity of the substrate. In Fig. 3(a), the minimum k along the [001] crystalline direction is positive when the exciting frequency and permittivity of the substrate are located in the regions labeled 1 and 2, which are surrounded by black and blue dashed lines. Although the k value is positive in region 3 where the ε_2 is more negative, i.e., the absolute value of ε_2 is larger, they do not satisfy that the arctanh function parameters must be between −1 and 1 (excluding −1 and 1) in Eq. (10), thus resulting in no excitation of l = 0 mode. Namely, as the ε_3 decreases, the minimum exciting frequency of l = 0 mode increases until it goes beyond RB 2. This explains that in the case of largely negative permittivity of substrate such as Au, the l =0 mode can not occur in RB 2. Moreover, it is found that the imaginary part of substrate permittivity, i.e., ε'', also affects the wavevector of the reoriented polaritons as shown in Fig. 3(b). Here we fix the real part of substrate permittivity i.e., ε' to −2, and change the ε'' from 10^{-5} to 1. The results show that in RB 2, the k is significantly reduced as ε'' is increased to 1.

To address the theoretical prediction above, we investigate the analytical dispersion of HPhPs in the 100-nm-thick α-MoO_3 slab when it is placed on the top of the SiC and Au substrates, respectively. Meanwhile, the results are compared with the air substrate configuration. Figure 4(a) shows the dispersion of propagating HPhPs along both in-plane crystalline directions ([100] and [001], corresponding to the x and y axes) in the air substrate configuration. The air-embedded α-MoO_3 slab supports the l =0 mode along the [100] direction, while there are no polaritonic modes along the [001] direction in the RB 2, agreeing with our analysis above. In the RB 3, the lowest order of polaritonic mode is l = 1, hence it

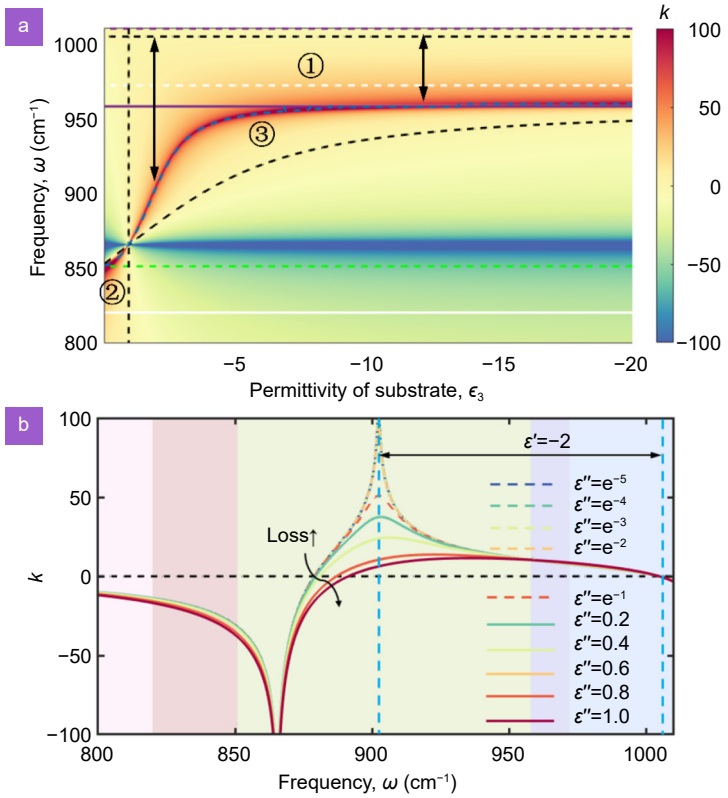

Fig. 3 | Minimum *k* of the excited *l* = 0 mode along the [001] crystalline direction, i.e., *y* axis. (**a**) The permittivity of the substrate is purely real. Dashed lines indicate the LO phonon frequency along the *x*- (white), *y*- (green) and *z*- (purple) directions and solid lines represent the TO phonon frequency along the *y*- (green) and *z*- (purple) directions. The black arrows show the excitation region of reorientated polaritons, which are surrounded by black and blue dashed curves and are labeled as 1 and 2. (**b**) The effect of the dissipation of substrate on the *k* of reorientated polaritons. The region where reorientated polaritons can be excited is bounded by the blue dashed lines. The thickness of the α-MoO_3 slab is fixed to 100 nm.

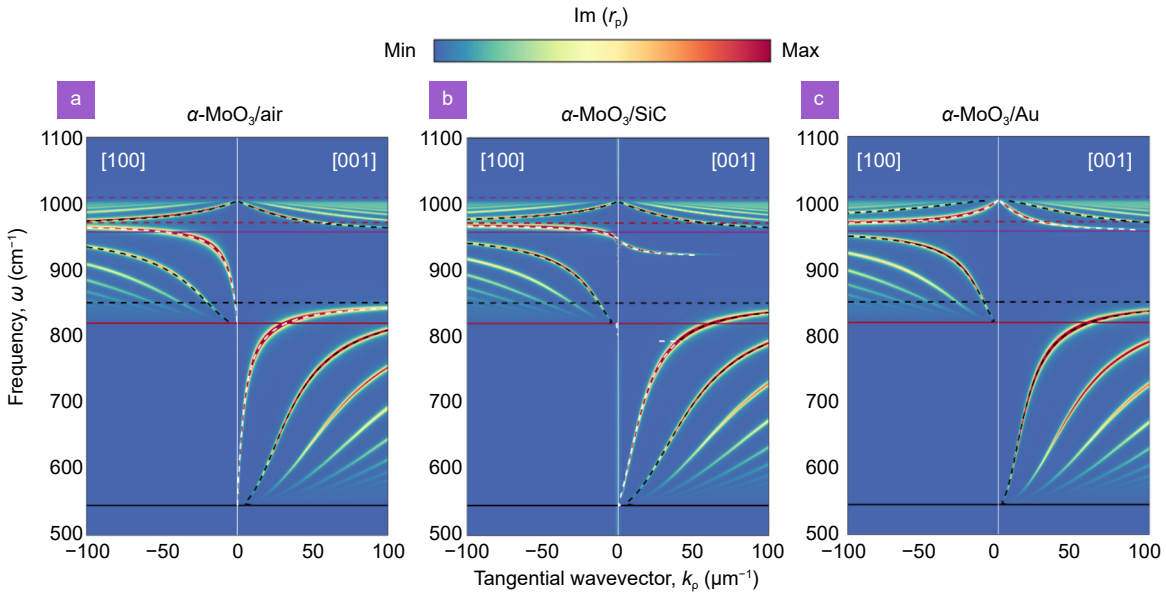

Fig. 4 | Dispersion of PhPs in α-MoO_3 slab with a thickness of 100 nm placed on the top of different substrates: (**a**) air; (**b**) SiC; (**c**) Au along the *x* (Left) and *y* (Right) directions. Dashed lines indicate the LO phonon frequency and solid lines represent the TO phonon frequency along the *x*- (red), *y*- (black) and *z*- (purple) directions. The false color plot displays the imaginary part of the Fresnel coefficient, r_p (ω, k), obtained from the transfer-matrix method (see details in the Supplementary information), which illustrates the polaritonic dispersion.

suppresses the excitation of the l = 0 mode. Replacing air with SiC, the propagating direction of the l = 0 mode is observed along the [100] direction between the LO phonon frequency of α-MoO_3, ω_{LO} = 963 cm^{-1} and phonon frequency of SiC, ω_0 = 948.6 cm^{-1} at which Re (ε_3) = −1. On the other hand, the l = 0 mode emerges along the [001] direction, namely, the forbidden direction below ω_0, i.e., when Re (ε_3) < −1 in Fig. 4(b). For the case of Au substrate, the lowest mode in RB 1 and RB 2 is l =1 mode due to the influence of the generated image charge[51] while in RB 3 it is l =0 mode due to largely negative permittivity of Au. Compared with air or SiC substrates, Au can excite the l =0 mode of the α-MoO_3 slab in RB 3 in Fig. 4(c).

To further study the HPhPs for different substrates, the IFC of the HPhPs dispersion relation is plotted in the k_x-k_y momentum space and compared to the false color plot of Im (r_p (k_x, k_y)). Exhibiting a hyperbola-shaped curve, the IFC of air substrate case gives rise to the propagation of hyperbolic polaritons within hyperbolic sectors between asymptotes, which are defined as $k_y = \pm\sqrt{|\varepsilon''_{xx}/\varepsilon''_{yy}|}k_x$, centered along the [100] crystalline direction (Fig. 5(a)) at an incident frequency, ω = 936 cm^{-1}, while it leads to a reorientation of the propagation direction of hyperbolic polaritons, rotating from the [100] direction to the [001] direction in the α-MoO_3/SiC heterostructures (Fig. 5(b)). Then, at another incident frequency, ω = 989 cm^{-1} (in RB 3), the shape of the IFC of the in-plane polaritonic mode is elliptical as shown in Fig. 5(c). However, the lowest order polariton changes from l =1 mode to l = 0 mode when the substrate is placed by Au, as shown in Fig. 5(d). To further validate these findings, the full-wave numerical simulations are performed, below which a vertically oriented electric dipole, acting as the polaritonic source, is placed on the top of the heterostructures. For the individual α-MoO_3 slab (Fig. 5(e)), HPhPs are propagating with concave wavefronts within hyperbolic sectors centered along the [100] directions. However, in α-MoO_3/SiC system (Fig. 5(f)), we observe HPhPs propagating with concave wavefronts within hyperbolic sectors centered along the [001] direction, which is the intrinsically forbidden polaritonic direction in a single slab of α-MoO_3. The results of the corresponding Fourier transform also reveal a 90° rotation of the major axis of the polaritonic IFC. These demonstrate that the directional propagation of in-plane HPhPs in α-MoO_3 slab can be effectively engineered along the previously forbidden direction. So far, there are two types of hyperbolic polaritons: volume-confined hyperbolic polaritons (v-HPs) and surface-confined hyperbolic polaritons (s-HPs). The v-HPs propagate directionally inside the crystal with a purely real-value out-of-plane wavevector[52]. By contrast, the s-HPs decay exponentially in the direction perpendicular to the interface[53]. Hence, the value of the out-of-plane wavevector is purely

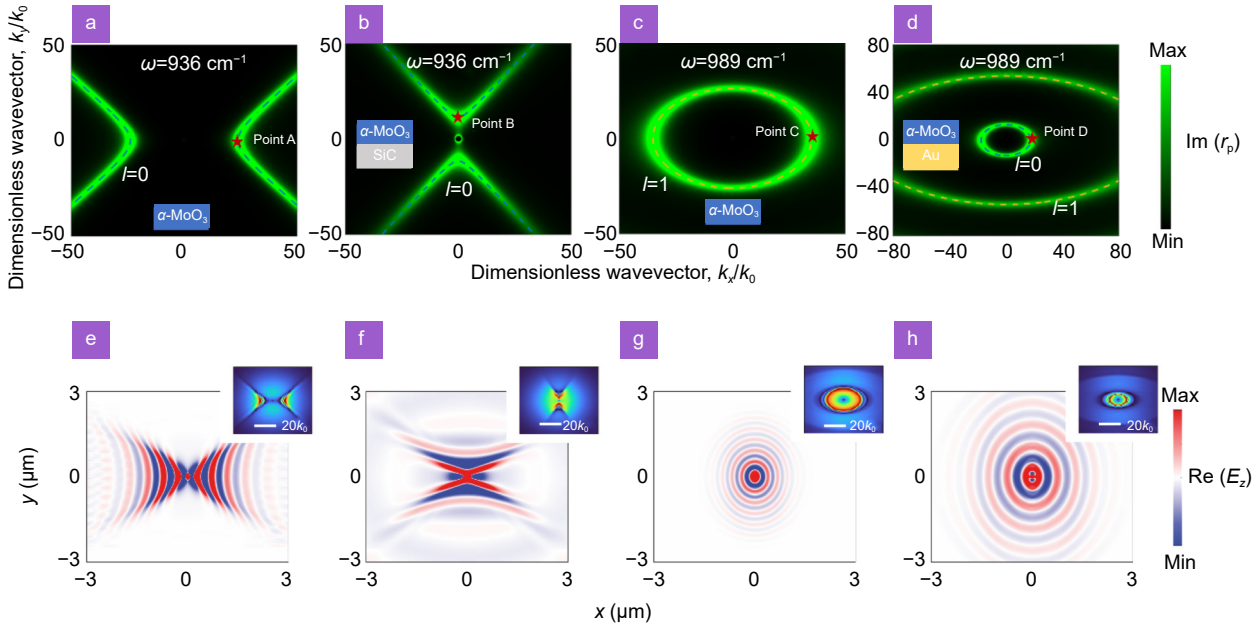

Fig. 5 | Dispersion and corresponding Im(r_p) of PhPs in a 100-nm-thick α-MoO_3 slab for air (**a**) and (**c**), SiC (**b**), and Au (**d**) substrates at different frequencies. At an incident frequency of 936 cm^{-1}, the principal axis of the hyperbola-like curves lays along the [100] direction (a) while it is along [001] direction (b) when adopting SiC substrate. Dashed curves are calculated analytically from Eq. (2), and the blue and yellow curves present l = 0 and l = 1 modes, respectively. (**e**–**h**) The simulated near-field distribution, Re (E_z), is excited by an electric dipole on the α-MoO_3 slab. The insets are the corresponding dispersions obtained by the Fourier transform of the electric distribution Re (E_z).

imaginary.

To study reoriented hyperbolic polaritons in the α-MoO_3/SiC and α-MoO_3/Au heterostructures, we first visualize the cross-sectional polariton field distribution. The electric-field map corroborates the existence of the v-HPs (Fig. 6(a) and 6(c)), consistent with what has been reported in prior works[5]. For the electric field in Fig. 6(b), corresponding to l = 0 mode in the α-MoO_3/SiC heterostructure, we cannot directly distinguish the type of hyperbolic polaritons due to the lack of exponentially decaying features away from the air/α-MoO_3 interface (z > 0). Therefore, we pay attention to the out-of-plane wavevector, q_{ez}[47,54]. Figure 7 shows the real and imaginary parts of q_{ez}, for incident frequency ω = 936 cm^{-1} and 989 cm^{-1}. It is found that for Point A (Fig. 7(a)), the q_{ez} is the real part dominated and its imaginary part is negligibly small, consistent with the feature of v-HPs. For Point B (Fig. 7(b)), the q_{ez} is imaginary part dominated, yielding the decay away from the interface. Thus, HPhPs along the [001] α-MoO_3 crystalline direction show surface-confined propagation. By contrast, the q_{ez} with ω = 989 cm^{-1} (Fig. 7(c) and 7(d)) is always the real part dominated in the whole k_x-k_y momentum space, ensuring the propagating feature inside the α-MoO_3 crystal. Hence, the l = 0 mode in the α-MoO_3/Au heterostructures is also v-HPs.

Effect of substrate with negative permittivity on NFRHT at various gap width

The substrate media have an obvious influence on the HPhPs excited in the α-MoO_3 crystal. In contrast to far-field thermal radiation, evanescent waves coupling between two bodies with subwavelength separation distance can assist photons to tunnel through the vacuum gap (i.e., photon tunneling), yielding a radiative heat flux that can exceed the blackbody limit by several orders of magnitude[55–61]. NFRHT has inspired a lot of research interest for its fundamental scientific relevance and technological application, including thermal rectification, thermal transistors, thermophotovoltaics, and photonic cooling[62–64], etc. To benefit these potential applications, continuous efforts have been devoted to exploring polaritonic modes that could intensify photon tunneling and control thermal radiation. Recently, researchers have found that the hybridization of different kinds of polaritons provides an exciting paradigm to modulate and control polaritons[65,66]. Inspired by this concept, many interesting ideas have been put forward in recent years. To date, most proposals for hybridization of polaritons rely strongly on suspended structures, ignoring the possible effects of substrates and not considering experimental implementations. Besides, the effect of the reorientation of hyperbolic polaritons in vdW crystal with substrates

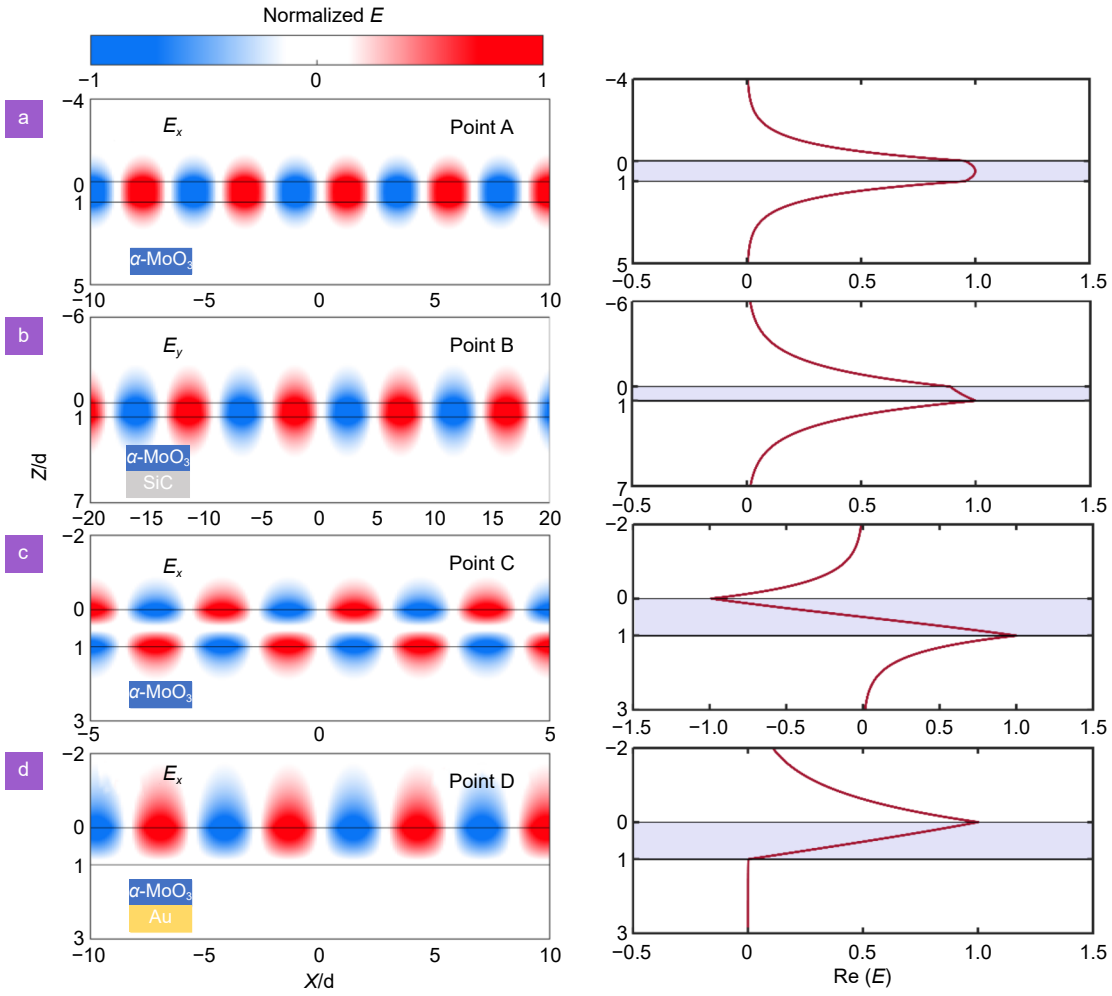

Fig. 6 | Left: the normalized cross-sectional near-field distribution of the HPhPs propagating along the surface. Right: corresponding field profile at *x* = 0. Points A-D come from Fig. 5. Differently, (**a**) and (**c**) adopt air substrate while (**b**) and (**d**) correspond to SiC and Au substrates. Calculate the real part of *x*-component of the electric field distribution, Re (E_x) is shown for Points A, C, and D, while the real part of the *y*-component of the electric field distribution, Re (E_y) is presented for Point B. The E_x and E_y are normalized by the corresponding maximum value, and the *x*-axis and *z*-axis are normalized by the thickness of the film. The black solid lines denote the air / α-MoO_3 interfaces and α-MoO_3 / substrate interfaces.

remains unexplored. To address this issue, we investigate the influence of polaritonic reorientations induced by substrates on NFRHT between heterostructures by applying the fluctuation-dissipation theorem.

We consider the NFRHT between two aligned heterostructures with the temperatures $T_{1(2)}$ = 300 (299) K and vacuum gap d. Each heterostructure consists of a thin α-MoO_3 slab with a thickness of t, and a substrate with infinite thickness as shown in Fig. 8(a). In this section, we focus on the analysis of the radiative heat flux (RHF), Q, which is given by[67,68]:

$$Q = \int_0^\infty q(\omega)\,\mathrm{d}\omega = \frac{1}{8\pi^3}\int_0^\infty \left[\Theta(\omega, T_1) - \Theta(\omega, T_2)\right]\mathrm{d}\omega \times \int_{-\infty}^{\infty}\int_{-\infty}^{\infty} \xi(\omega, k_x, k_y)\,\mathrm{d}k_x\mathrm{d}k_y\,, \tag{11}$$

where $\Theta(\omega, T) = \hbar\omega/\left(\mathrm{e}^{\hbar\omega/k_\mathrm{B}T} - 1\right)$ is the mean energy of a Planck oscillator at angular frequency ω and temperature T. $\xi(\omega, k_x, k_y)$ is the PTC, which is expressed as[65,66]

$$\xi(\omega, k_x, k_y) = \begin{cases} \mathrm{Tr}\left[\left(\boldsymbol{I} - \boldsymbol{R}_2{}^*\boldsymbol{R}_2 - \boldsymbol{T}_2{}^*\boldsymbol{T}_2\right)\boldsymbol{D}\left(\boldsymbol{I} - \boldsymbol{R}_1{}^*\boldsymbol{R}_1 - \boldsymbol{T}_1{}^*\boldsymbol{T}_1\right)\boldsymbol{D}^*\right], k < k_0 \\ \mathrm{Tr}\left[\left(\boldsymbol{R}_2{}^* - \boldsymbol{R}_2\right)\boldsymbol{D}\left(\boldsymbol{R}_1 - \boldsymbol{R}_1{}^*\right)\boldsymbol{D}^*\right]\mathrm{e}^{-2|k_{z0}|d}, k > k_0 \end{cases}, \tag{12}$$

where $k_{z0} = \sqrt{k_0^2 - k^2}$ is the perpendicular wavevector component in vacuum and * denotes the complex conjugate. $\boldsymbol{R}$ and $\boldsymbol{T}$ are matrixes of Fresnel reflection and transmission coefficient for a plane wave incidence from vacuum to medium 1 or 2, respectively, and have the following forms:

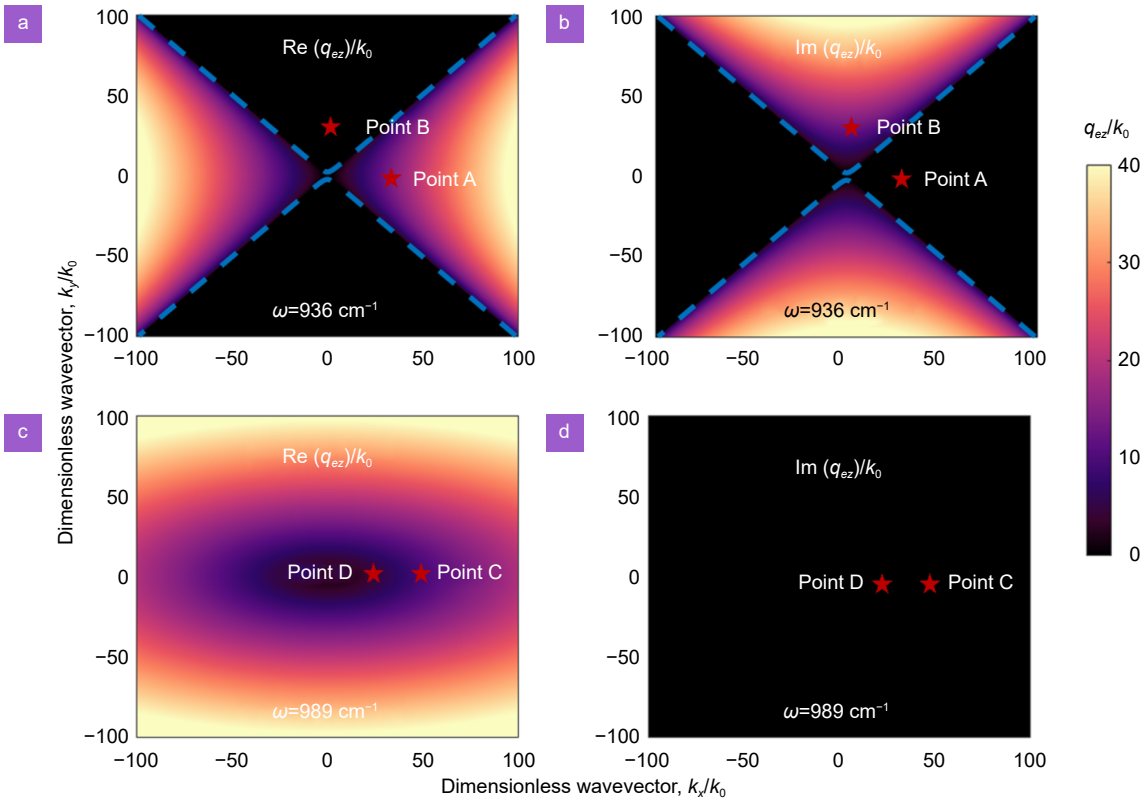

Fig. 7 | The calculated real and imaginary parts of q_{ez} at ω = 936 cm^{-1} in (**a**) and (**b**), and ω = 989 cm^{-1} in (**c**) and (**d**). An imaginary part-dominated q_{ez} represents the decaying along the direction perpendicular to the interface while the real part-dominated one corresponds to phase oscillation.

$$\boldsymbol{R}_{1,2} = \begin{bmatrix} r_{ss}^{1,2} & r_{sp}^{1,2} \\ r_{ps}^{1,2} & r_{pp}^{1,2} \end{bmatrix}, \boldsymbol{T}_{1,2} = \begin{bmatrix} t_{ss}^{1,2} & t_{sp}^{1,2} \\ t_{ps}^{1,2} & t_{pp}^{1,2} \end{bmatrix}. \quad (13)$$

The 2×2 matrix $\boldsymbol{D}$ describes the Fabry-Perot-like denominator, defined as $\boldsymbol{D} = (\boldsymbol{I}-\boldsymbol{R}_1\boldsymbol{R}_2 e^{2ik_{z0}d})^{-1}$.

To reveal the effect of the reorientation of HPhPs on NFRHT, we adopt two kinds of practical substrates: SiC and Au and compare them with the individual slab configuration. Figure 8(b) shows the radiative heat flux as a function of the vacuum gap width, d in three kinds of structures: (I) bare α-MoO_3 slab, (II) α-MoO_3 / SiC heterostructure, (III) α-MoO_3 / Au heterostructure. The thickness of the α-MoO_3 slab is fixed to 20 nm. As a benchmark, Fig. 8(b) shows the increase of near-field RHF increases by several orders of magnitude over the blackbody limit due to the evanescent contribution. The blackbody limit at room temperature can be given by $h = \sigma_B T^4 = 6.093$ Wm^{-2}, where σ_B is Stefan-Boltzmann constant (gray dashed line in Fig. 8(b)). In particular, the results show that the total heat flux of each configuration is enhanced up to 2000-fold above the blackbody limit at d = 10 nm. To directly exhibit the enhancive and annihilative effect of the substrates, we define the relative enhancement coefficient η to describe the ratio of heat fluxes for the case with the substrate to that for suspended α-MoO_3 slabs as:

$$\eta = \frac{Q_{sub}}{Q_{air}}, \quad (14)$$

where Q_{sub} and Q_{air} refer to the radiative heat flux with and without substrates, respectively.

Further, we observe that the results for SiC and Au substrates exhibit different features when the vacuum gap increases. For the configuration of α-MoO_3 / SiC heterostructure, when d is less than 25 nm (Region I), the radiative energy exchange is basically the same as that of bare α-MoO_3 slab, independent on the type of substrate. This is because the films in this case are in effect bulk materials when the nanoscale gap width becomes comparable to or smaller than the film thickness[69]. In contrast, even when the vacuum gap is smaller than the thickness of the α-MoO_3 film in the α-MoO_3 / Au heterostructure, the α-MoO_3 film can still not be regarded as a bulk material. It can be seen from Fig. 8(c) that the Au substrate always suppresses the radiative heat transfer and the suppressive effect strengthens as the vacuum gap width increases. SiC substrate suppresses the radiative energy transport in Region II (25 nm < d < 210 nm),

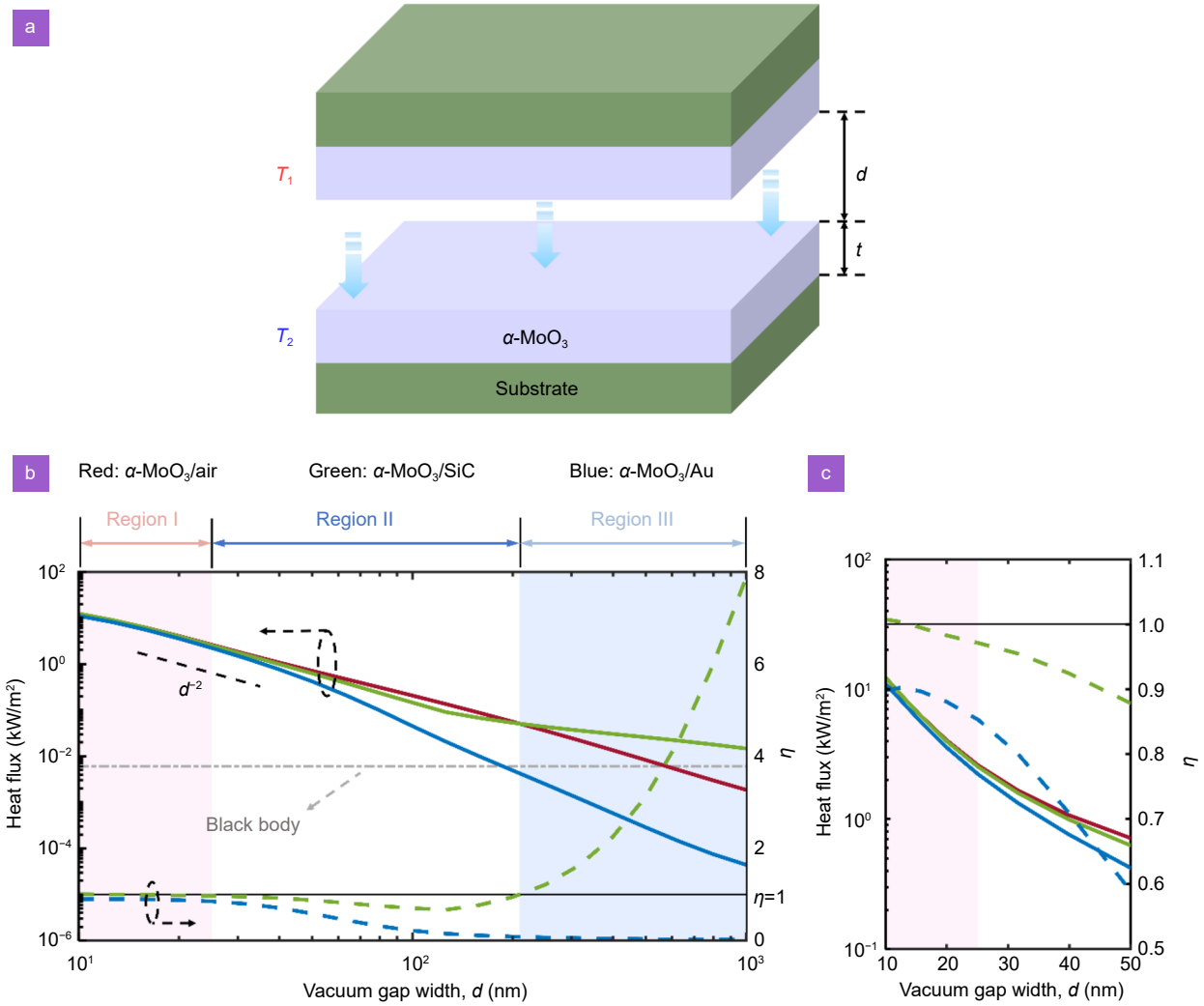

Fig. 8 | Effect of substrate on NFRHT: (**a**) Schematic of NFRHT between two heterostructure systems composed of α-MoO_3 slab with a thickness of t and practical substrates: SiC and Au. The vacuum gap width is d. The top structures is the emitter with a high temperature T_1 (300 K) and the structure below the vacuum gap is receiver with a low temperature T_2 (299 K). (**b**) The RHF (left) and relative enhancement coefficient η (right) for three kinds of structures as functions of vacuum gap width, d at thickness of α-MoO_3 slab t =20 nm. The structures studied include (I) the individual α-MoO_3 slab, (II) heterostructure consisting of α-MoO_3 and SiC, and (III) heterostructure consisting of α-MoO_3 and Au. The gay dotted line denotes the black body limit. (**c**) The enlargement of panel (b) for small gap size. According to the relative enhancement coefficient of SiC substrate, the whole region is divided into three parts: Region I ($\eta \approx 1$); Region II annihilation ($\eta < 1$); Region III enhancement ($\eta > 1$).

while the effect of SiC substrate on NFRHT transforms from suppression to enhancement as d exceeds 210 nm (Region III). In particular, at d = 1000 nm, the total heat flux of α-MoO_3 / SiC heterostructure system yields 14.7 W/m^2, which is 8 times larger than that of α-MoO_3 / air system.

To reveal the physical origin of the enhancement effect at a large vacuum gap width, we calculate the spectral heat flux for three kinds of structures at d =1000 nm as shown in Fig. 9(a). Note that at the nanoscale, the main contribution to NFRHT comes from the excitation of surface-confined or volume-confined modes inside the RBs. However, at larger gap width, i.e., far-field region, it is the propagating wave that dominates. As shown in Fig. 9(a), there are three spectral peaks for bare α-MoO_3 slab and one spectral peak for α-MoO_3 / Au system and these peaks are all located inside the RBs. The phonon tunneling between two α-MoO_3 heterostructures (i.e., the PTC) can explain the origin of these modes. Figure 10(a) and 10(b) represent the PTC of the first and second peaks of α-MoO_3 / SiC system. One can see that the hyperbolic features come from the coupling of the epsilon near pole modes and hyperbolic volume-confined modes. As shown in Fig. 10(c), the PTC at the spectral peak of α-MoO_3 / Au system exhibits elliptical topology, indicating that it results from the coupling the

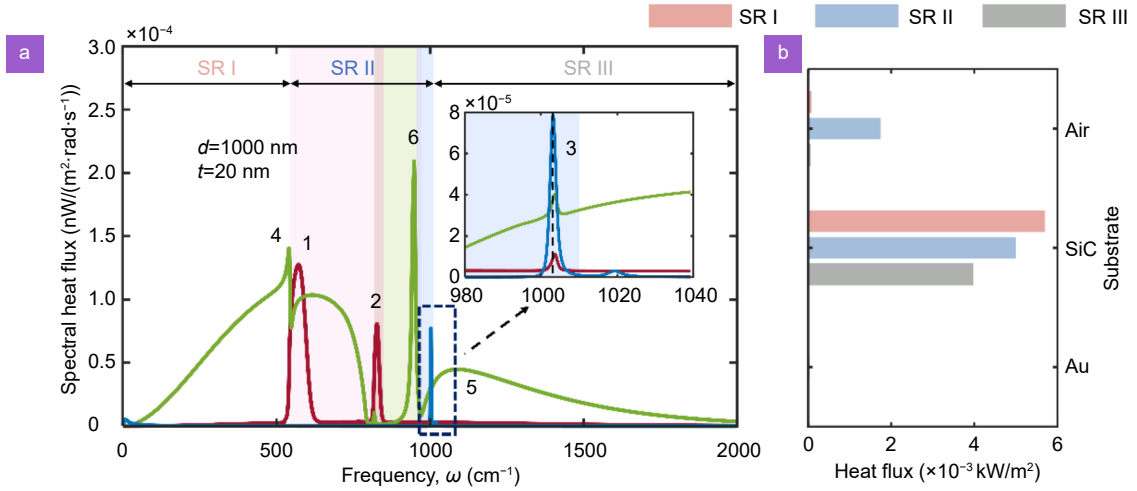

Fig. 9 | (**a**) Spectral heat flux for a vacuum gap size d =1000 nm at a thickness of α-MoO_3 slab t =20 nm. The SR II represents the inside of RBs, and the SR I and SR III denote the outside of RBs. (**b**) The heat flux from three spectral regions for the three structures.

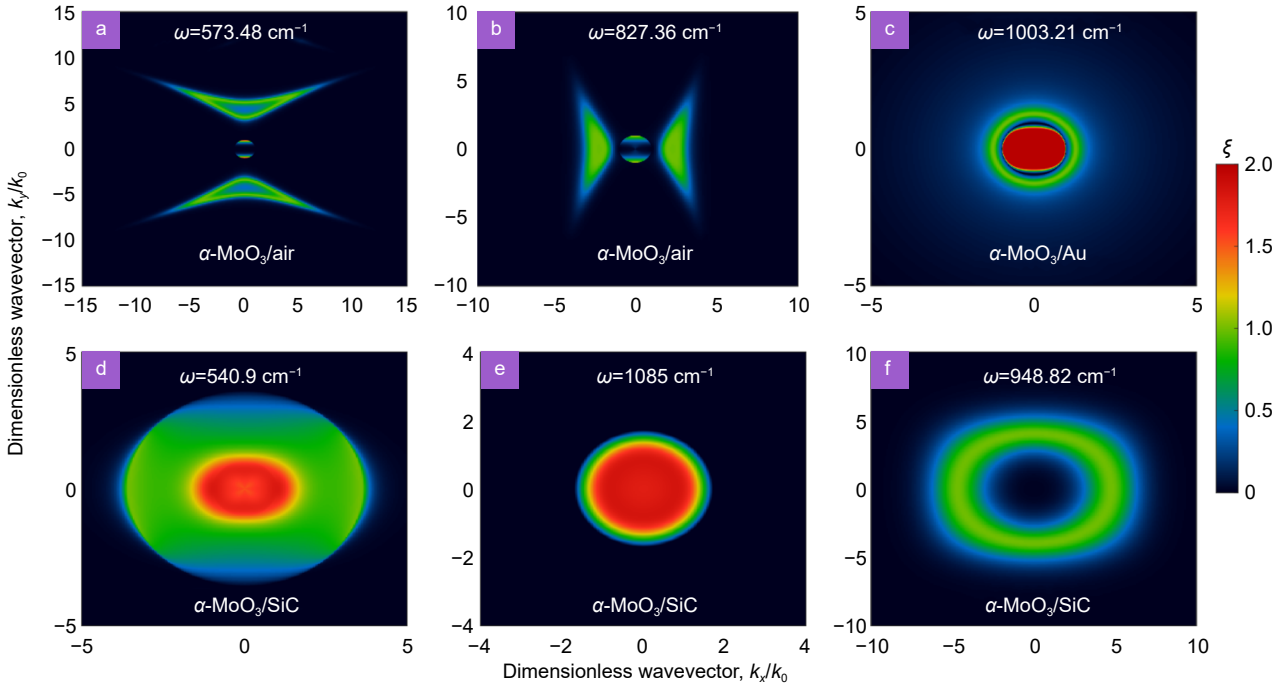

Fig. 10 | In-plane PTC at frequencies corresponding to the peaks 1-6 labeled in Fig. 9(a) for the α-MoO_3 /substrate heterostructure and suspended configurations.

elliptical volume-confined modes. Therefore, combining with Fig. 9(b) and Fig. 10(a–c), one can see that the contribution to the NFRHT between two heterostructures mainly comes from the inside of RBs for α-MoO_3 / air and α-MoO_3 / Au systems. However, it becomes complicated for α-MoO_3 / SiC system. It is outside of RBs that dominates in energy exchange between two α-MoO_3 / SiC heterostructures at large vacuum gap width, i.e., 1000 nm. As shown in Fig. 10(d) and 10(e), the evanescent wave ($k > k_0$) and propagating wave ($k < k_0$) outside of RBs both make contributions. Particularly, in RB 2, the PTC of Fig. 10(f) exhibits the closed features, suggesting that the phonon tunneling is mainly affected by the modes excited by SiC substrate. Therefore, we can get a conclusion that the SiC substrate amplifies the enhancive effect on NFRHT compared with the configuration without substrate at a large vacuum gap.

Effect of the thickness of α-MoO_3 slab on NFRHT

In this section, we fix the vacuum gap d = 20 nm. Fig. 11(a) shows the RHF as a function of thickness of α-MoO_3 slab, t. It is obviously seen that in the case of large

thickness, the effect of the substrates, i.e., SiC and Au, on radiative heat transfer is negligible, since the slabs can be regarded as bulk materials. As a comparison, the critical thickness of SiC substrate (t = 150 nm), where the effect of the substrate on radiative heat transfer is negligible, is smaller than that of Au substrate (t = 300 nm). Besides, we obverse that compared with the suspended scenario, the Au substrate always suppresses the radiative heat transfer when t is less than the critical thickness while the SiC substrate slightly enhances RHF as t is larger than 25 nm and smaller than the critical thickness. When t < 25 nm, the SiC substrate plays a negative role in enhancing RHF. The spectral analysis allows us to understand the mechanism for the suppressive effect on NFRHT. Fig. 11(b) shows the spectral RHF for two substrate scenarios at d = 20 nm has a prominent feature with new peaks at 939.6 cm^{-1} and 961.4 cm^{-1} for SiC substrate and 978.3 cm^{-1} for Au substrate. Moreover, the spectral heat flux of SiC substrate is less than that of the suspended scenario in a spectral region from 766 cm^{-1} to 927 cm^{-1}, covering RB 1 and RB 2.

The mechanisms by which substrate affects the radiative heat transfer can be explored by phonon tunneling between the two α-MoO_3 heterostructures (i.e., the PTC). Here, we focus on incident frequencies: 780 cm^{-1} (RB 1), 900 cm^{-1} (RB 2) and two peaks mentioned above, 939.6 cm^{-1} and 961.4 cm^{-1}. At the frequency of 780 cm^{-1}, the real part of the permittivity of SiC is positive, resulting in the excitation of the l = 0 mode of HPhPs, as shown in Fig. 12(a). The bright branches represent the photon tunneling, originating from the coupling of PhPs between two individual heterostructures. Here, we obtain the dispersion relation from $1-r^{pp}r^{pp}e^{2ik_{z0}d}=0$[70], since the contributions to NFRHT in nonmagnetic materials are dominated by transverse magnetic waves, i.e., p-polarized waves[65–67,71]. The dispersion curves are hyperbolic and unambiguously located in the bright contour of mode branches. Compared with the suspended case in Fig. 12(e), the bright hyperbolic branches are extended to a larger range of wavevectors ~300 k_0 for SiC substrate scenario. Figure 12(b) and 12(f) show the PTC at the frequency of 900 cm^{-1} for suspended and SiC substrate cases, respectively. The bright branches match well with the dispersion curves, yielding hyperbolic features. Combined with Fig. 4(a), it can be found that the hyperbolic bright branches in Fig. 12(b) represent the l = 1

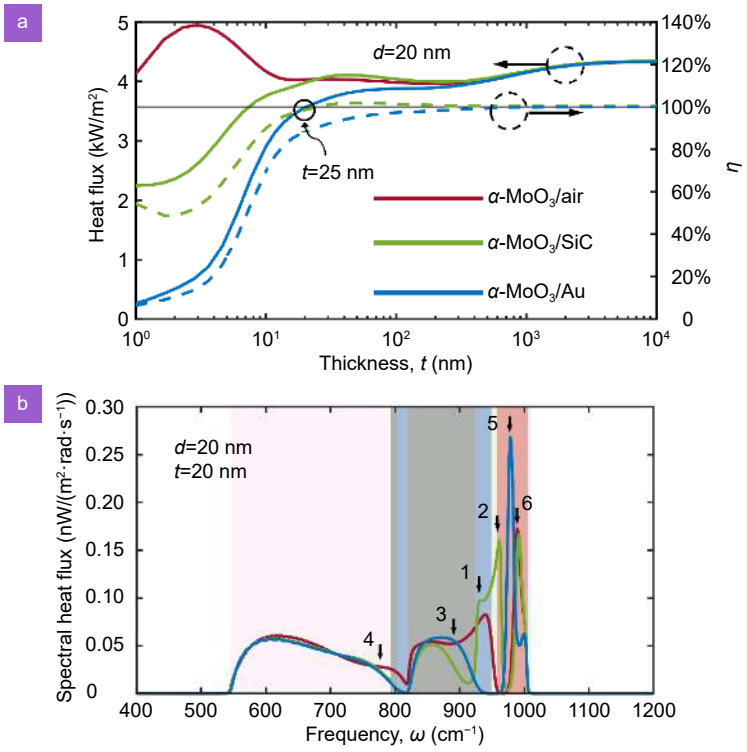

Fig. 11 | (**a**) The radiative heat fluxes (left) and relative enhancement coefficient η (right) for three kinds of structures as functions of the thickness of α-MoO_3 at a vacuum gap d =20 nm. (**b**) Spectral heat fluxes for three kinds of structures, at t = 20 nm. The dark blue and gray shaded region indicate the reorientation and annihilation of the l = 0 mode in α-MoO_3 / SiC heterostructure, respectively. The red shaded region represents the excitation of the l = 0 mode in α-MoO_3 / Au heterostructure.

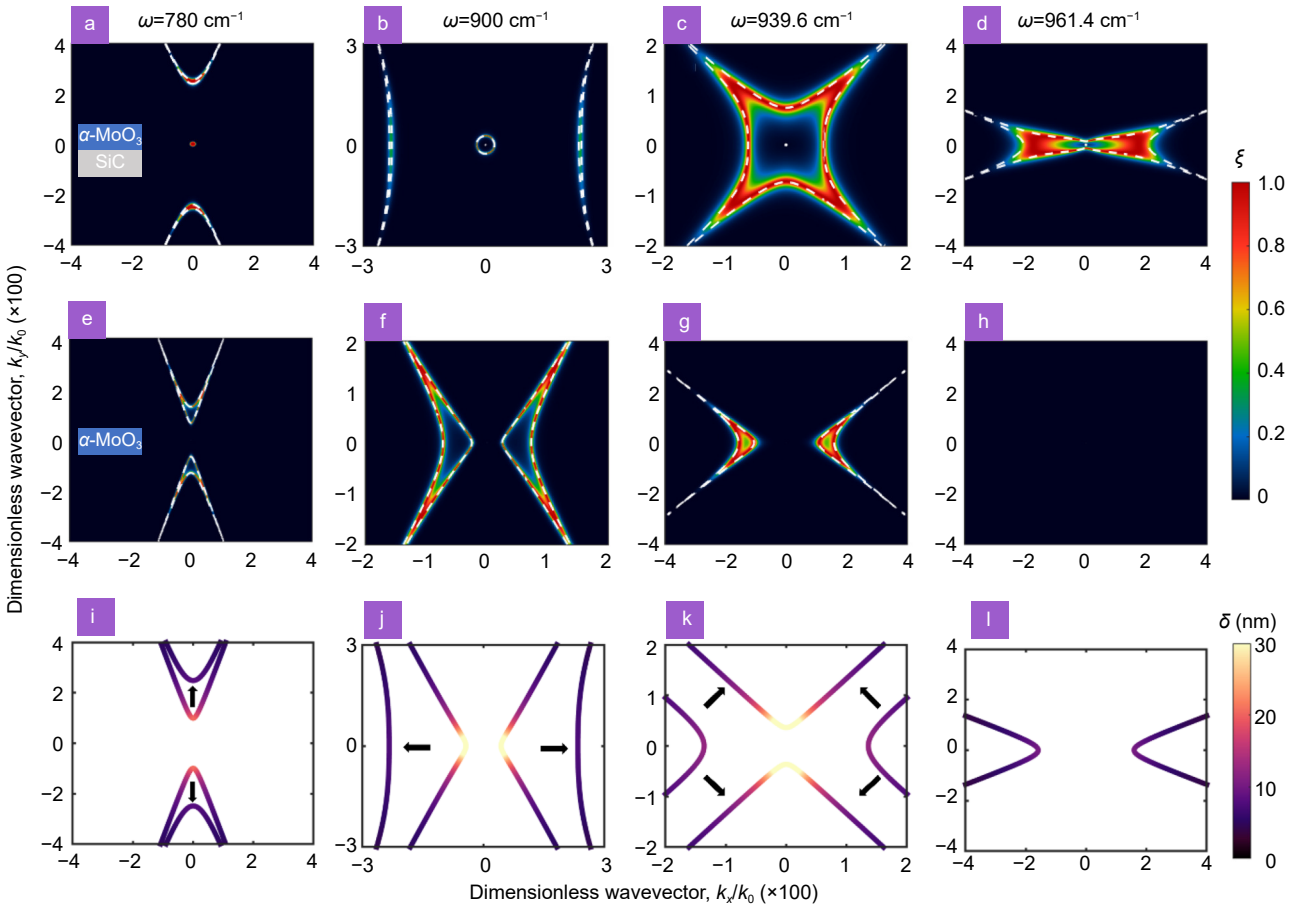

Fig. 12 | In-plane PTC for α-MoO_3 / SiC heterostructure (**a–d**); the individual α-MoO_3 slab (**e–h**) at frequencies of the peaks 1–4 labeled in Fig. 11(b). (**i–l**) denote the attenuation length of the fundamental mode (l = 0). The arrows indicate the movement of dispersion curves when the α-MoO_3 slab is placed on the top of SiC substrate. The white dashed curves indicate the symmetric and anti-symmetric branches of the coupled modes.

mode due to $\mathrm{Re}(\varepsilon_1) + \mathrm{Re}(\varepsilon_3) < 0$. Moreover, the wavevector region is also increased to ~250 k_0 compared with ~100 k_0 in the suspended scenario. Whether the increase of wavevector leads to an enhancement or a weakening of spectral RHF can be explained via the coupling of polaritons. Note that the enhancement of NFRHT is dominated by increased photon tunneling channels, which is closely related to the coupling of the surface modes. Note that for small attenuation length, the evanescent wave is easily filtered by the vacuum gap, so the system consisting of two individual surfaces no longer stimulates the obvious polaritonic coupling effect, resulting in the descending of radiative tunnels. Therefore, the strength of coupling depends on the attenuation length and vacuum gap. Previous studies[68,71] have suggested that for two bodies with gap distance d, the maximum accessible wavenumber for photon transmission is $\sim \frac{1}{d}$. The attenuation length of HPhPs is $\delta = \frac{1}{\mathrm{Im}\,(k_{z0})}$. We know that $\mathrm{Im}\,(k_{z0}) \sim k$ is accessible for large wavevector, so it can be understood that for the maximum accessible wavenumber, the attenuation length is on the order of the gap size[72]. Consequently, only when the attenuation length of the polaritonic mode is larger than the gap distance can the mode make an obvious contribution to the enhancement of total heat flux. As shown in Fig. 12(i), the hyperbolic branches move toward the larger-wavevector ones after adopting the SiC substrate. Meanwhile the attenuation length decreases, yielding a weakened coupling effect. Therefore, it explains why the spectral heat flux drops from 0.0276 nW/(m²·rad·s⁻¹) to 0.0215 nW/(m²·rad·s⁻¹) as the α-MoO_3 crystal is placed on the top of SiC substrate. For the case of the 900 cm⁻¹ (shown in Fig. 12(j)), the attenuation length of l = 0 mode in the suspended scenario is larger than vacuum gap (20 nm), while that of l = 1 mode in the SiC substrate scenario is smaller than vacuum gap, weakening the radiative heat flux. The new spectral heat flux peaks

located at 939.6 cm^{-1} and 961.4 cm^{-1} originate from the reorientation of HPs. At 939.6 cm^{-1} where $Re(\varepsilon_1) + Re(\varepsilon_3)) < 0$, the direction of the propagating in-plane $l = 0$ mode is rotated by 90°(thus occurring along the intrinsically forbidden direction). Additionally, because of the coupling between the evanescent fields of $l = 0$ mode in the top and bottom heterostructures, the surface mode would split into two resonant branches, i.e., the antisymmetric and symmetric modes, as shown in Fig. 12(c) and 12(g). The dispersion relations match well with the bright branches. Different from Fig. 12(g) where the antisymmetric and symmetric branches are located in the left and right parts of wavevector regions, these two resonant modes are split into the top and bottom parts, left and right parts of wavevector regions in Fig. 12(c). In terms of spectral radiative heat transfer, the reorientation of HPhPs improves the photon tunneling of the system due to stronger coupling in lower k_x-k_y wavevector regions as shown in Fig. 12(k). The other spectral heat flux peak is located at ω = 961.4 cm^{-1}, where $Re(\varepsilon_1) + Re(\varepsilon_3) > 0$. For the suspended scenario, the attenuation length of $l = 0$ mode is so small that the contribution to the radiative heat transfer is negligible (Fig. 12(h)). Although no rotation of $l = 0$ mode occurs, the SiC substrate provides a stronger surface state by reducing the wavevector, improving the photon tunneling of the system effectively as shown in Fig. 12(d). This is why the peak occurs.

For the Au substrate scenario, the new spectral heat flux peaks are located at 978.3 cm^{-1} and 1000 cm^{-1} as shown in Fig. 11(b). From the PTC shown in Fig. 13(a), we get that photon tunneling is dominated by the coupling between the evanescent fields of $l = 0$ mode in the top and bottom α-MoO_3 /Au heterostructures, which is attributed to the spectral heat flux peak. The coupling between $l = 1$ modes in the suspended scenario is so weak (shown in Fig. 13(c)) that the contribution to NFRHT is negligible. At a frequency of 989 cm^{-1}, the coupling effect is obvious in the case with or without Au substrate. However, there is only one resonant branch, matching well with the dispersion contour in Fig. 13(b). The blue dashed curve represents the in-plane elliptical IFC, which separates the antisymmetric and symmetric modes. Hence, the only branch is symmetric mode. Namely, the antisymmetric mode is suppressed. This also explains why the spectral heat flux in α-MoO_3 /Au heterostructure is less than that in the suspended scenario.

Effect of substrates on NFRHT along different crystalline directions of α-MoO_3 between heterostructures integrated with SiC and Au

Considering that α-MoO_3 exhibits different polaritonic

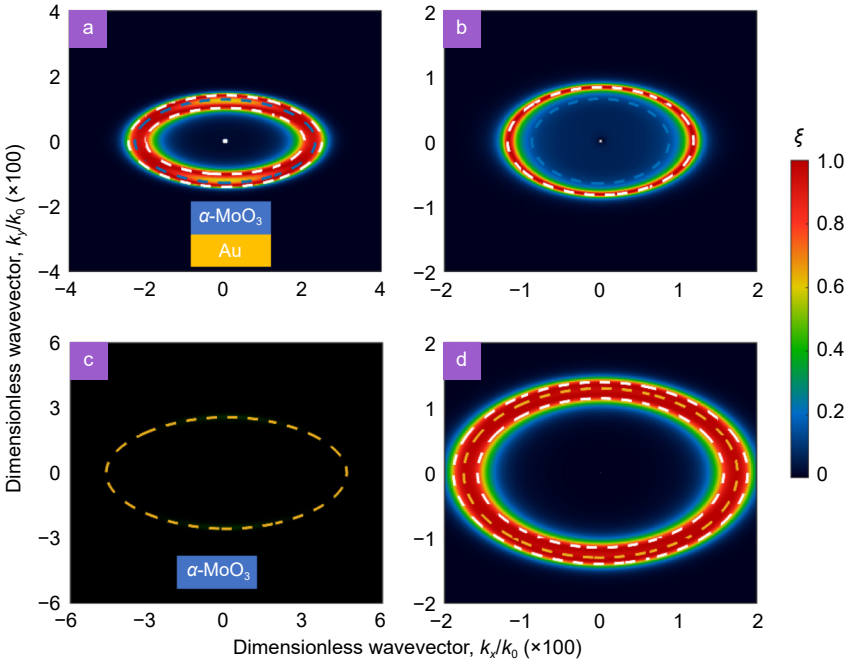

Fig. 13 | In-plane PTC for α-MoO_3 / Au heterostructure (**a**) and (**b**); the individual α-MoO_3 slab (**c**) and (**d**) at a frequency of the points 5 and 6 labeled in Fig. 11(b). The blue and yellow dashed curves represent the dispersion relation of the l = 0 and l =1 modes, respectively. The white curves denote the coupled symmetry and anti-symmetry modes.

properties along the three crystalline directions, it is worthwhile investigating the effect of substrates on NFRHT between heterostructures consisting of α-MoO_3 and substrate along different crystalline directions. We have discussed the heat flux along the [010] crystalline direction above. However, the heat flux along the [001] crystalline direction exhibits distinctive features, as shown in Fig. 14 in which the results are obtained with d = 20 nm. Note that in this section the [100], [010] and [001] crystalline directions correspond to the x, y and z axes in the Cartesian coordinate system, respectively. It is clear to see in Fig. 14(a) that once the thickness of α-MoO_3 slab exceeds 2.5 nm, the role of Au substrate turns to be enhancive effect and its heat flux is 1.5 folds of that of air scenario when t increases to 7 nm. SiC substrate keeps enhancing the radiative heat transfer until the substrate effect disappears (t > 300 nm). Particularly, in the case of 1 nm-thickness α-MoO_3, the heat flux with SiC substrate is more than 2 times as large as that of the air scenario. To explain the physical mechanism behind the enhancing effect, the spectral heat flux of 10 nm-thickness α-MoO_3 is chosen as shown in Fig. 14(b) and the inset shows the SiC and Au substrates improve radiative heat flux from 3.639 kW/m² to 5.2916 kW/m² and 5.015 kW/m², respectively. Compared Fig. 14(b) with Fig. 11(b) (heat flux along [010] crystalline direction), the maximum spectral heat flux peak moves toward lower frequency (redshift) and in the case of SiC and Au substrates, the contribution from RB 1 remarkably increases from a qualitative perspective, which attracts our attention. To further clarify the mechanism for the enhancement, the heat flux contribution from every region is calculated and shown in Fig. 14(c). The results exhibit that after the substrate is replaced with SiC or Au, the contribution from RB 1 significantly increases from 0.7033 kW/m² to 2.2858 kW/m² and 2.7018 kW/m², respectively. Meanwhile, its proportion of total heat flux increases from 19.33% to 43.20% and 53.87%, respectively,

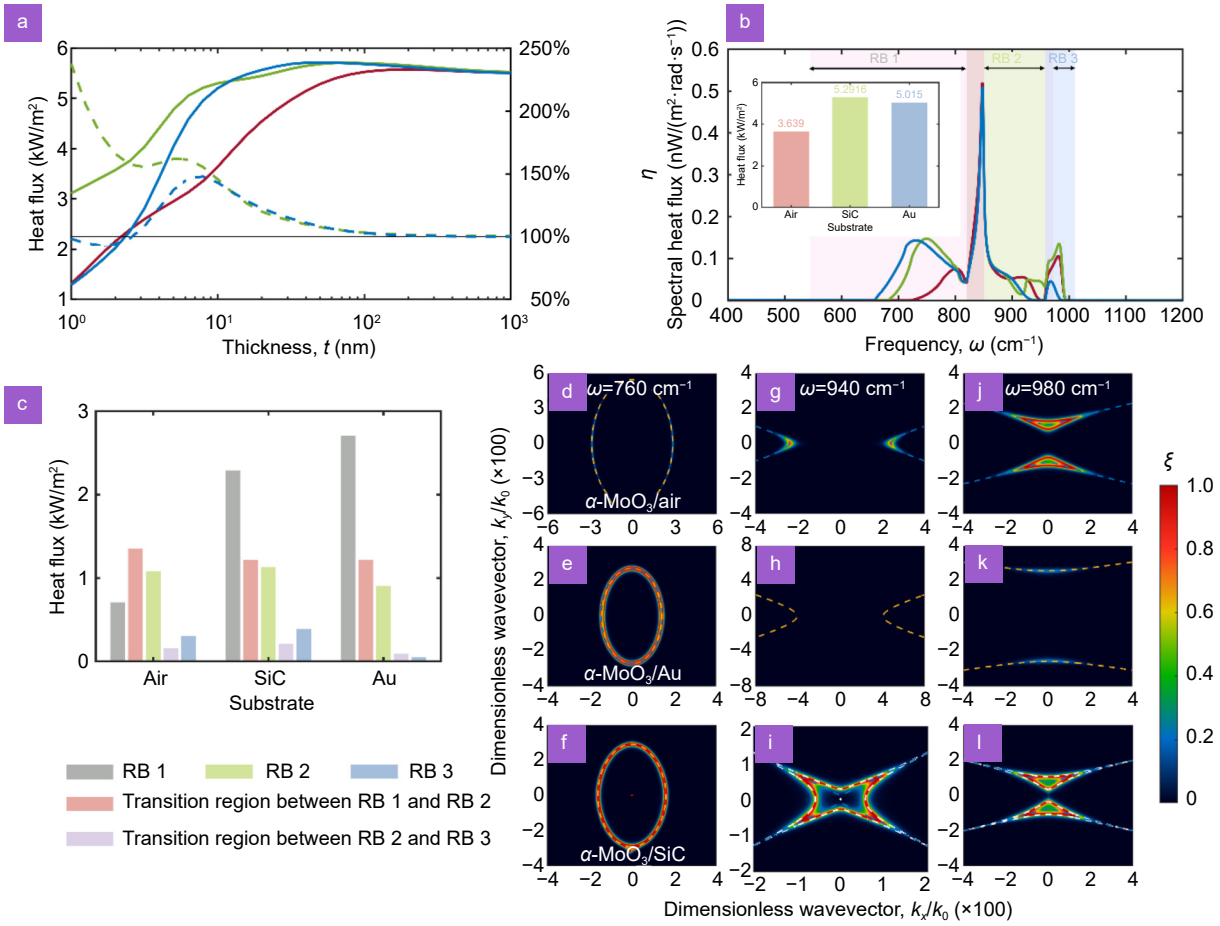

Fig. 14 | NFRHT along the [001] crystalline direction for d = 20 nm. (**a**) Left: radiative heat flux varies with the thickness of the α-MoO_3 slab for the cases with and without substrates. Right: the relative enhancement coefficient. (**b**) Spectral heat flux and total heat flux(inset) for the 10 nm-thickness α-MoO_3 slab. (**c**) Heat flux from every RB. In-plane PTC at incident frequency of 760 cm⁻¹ (RB 1) (**d–f**), 940 cm⁻¹ (RB 2) (**g–i**) and 980cm⁻¹ (RB 3) (**j–l**) for three structures: individual α-MoO_3 slab, α-MoO_3/ Au and α-MoO_3/ SiC heterostructures.

indicating its dominance. In addition, the heat flux from RB 3 slightly increases for SiC substrate while dramatically reduces for Au substrate. This phenomenon results from the rotation of the crystal optical axis direction. To be specific, the [001] crystalline direction becomes perpendicular to the surface after rotating 90° around the [100] crystalline direction, i.e., x axis, so that the heat flux is along the [001] direction. This leads to the IFC of PhPs being closed or elliptical in RB 1, while it being open or hyperbolic while that in RB 3. The coupling of PhPs depends on the polaritons in single slabs. We know that the substrate with negative permittivity can excite the l = 0 mode of elliptical PhPs, which can boost the phonon tunneling. The PTC in Fig. 14(d–f) shows the elliptical shape dispersion curves, and only the Au substrate excites the l = 0 mode, leading to the stronger coupling between the two individual heterostructures and the enhancement of heat flux in RB 1. It is noticeable that even though the SiC substrate excites l = 1 mode due to the positive permittivity at a frequency of 760 cm^{-1}, the strong coupling between PhPs in the emitter and the receiver also increases the spectral heat flux, yielding the enhanive effect. Focusing our attention on the RB 2, the reorientation of PhPs occurs for SiC substrate as shown in Fig. 14(i). Although the reorientation improves the spectral heat flux in the blue shaded region shown in Fig. 14(b), its narrow band limits the enhancive effect on the total heat flux. The largely negative permittivity of Au substrate suppresses the excitation of l = 0 mode, and makes l = 1 mode excited in higher momentum space as shown in Fig. 14(h) and 14(k), weakening the coupling of PhPs and decreasing the spectral heat flux. For RB 3, the positive permittivity of SiC leads to stronger coupling between l = 0 hyperbolic polaritons as shown in Fig. 14(l) and increases the photon tunneling.

Conclusions

In conclusion, we present a comprehensive study of the effect of negative permittivity substrate on the hyperbolic phonon polaritons. We have demonstrated the reorientation of the directional propagation of low-loss HPhPs in a natural hyperbolic crystal along intrinsically forbidden directions when the crystal is laid on a substrate with a moderate negative permittivity. In addition, we reveal that the substrate with negative permittivity can generate the fundamental mode which is suppressed in the configuration of the substrate with positive permittivity. Our results show that HPhPs propagate along the naturally forbidden [001] crystalline direction for fundamental polaritonic propagation in bare α-MoO_3 when it is placed on the top of SiC at ω = 936 cm^{-1}. The excitation of the fundamental mode with an elliptical isofrequency dispersion contour is realized at ω = 989 cm^{-1} when α-MoO_3 is placed on Au with large negative permittivity. The reoriented and excited fundamental modes are theoretically identified as s-HPs and v-HPs, respectively, via the electrical field distribution and the values of q_{ez}. Changing the local environment provides new opportunities for dynamically tuning PhPs at the nanoscale. Thanks to the active modulation of the electromagnetic state of PhPs via the blocal environment, we further investigate the effect of the polaritonic coupling between heterostructures integrated with different substrates on the radiative energy transport. The results show that the reorientation and excitation of the fundamental mode can further improve the NFRHT while the annihilation of the fundamental mode suppresses it. For two kinds of practical substrates: SiC and Au, the enhancement or suppression of radiative energy transport depends on the relative magnitude of the slab thickness and the vacuum gap width. When the nanoscale vacuum gap is smaller than the slab thickness, the nanofilms with and without substrates are as effective as bulk materials, yielding no effect of substrate on radiative energy transport. Finally, the effect of substrates on NFRHT along different crystalline directions is considered. In the case of heat flux along the [001] crystalline direction between two heterostructures integrated with SiC or Au, the spectral band of the excitation of the fundamental mode resulting from the negative permittivity substrates is shifted to RB 1, where the heat flux is greatly improved due to wider band. In this configuration, the contribution from RB 1 dominates and improves the enhancement effect of PhPs compared to the suspended configuration.

It should be pointed out that although α-MoO_3 is chosen for demonstration in this paper, the conclusions obtained apply to other vdW materials, such as α-VO_5 and hBN. Therefore, our findings promise new opportunities for actively modulating heat management at the nanoscale via tailoring the phonon polaritons. Furthermore, this study provides fundamentally relevant insights into understanding in-plane anisotropic polaritons of vdW materials.

References

1. Low T, Chaves A, Caldwell JD et al. Polaritons in layered two-

dimensional materials. *Nat Mater* **16**, 182–194 (2017).
2. Li M, Hu GW, Chen X et al. *Sci Adv* **8**, eadd6660 (2022).
3. Passler NC, Ni X, Hu GW et al. Hyperbolic shear polaritons in low-symmetry crystals. *Nature* **602**, 595–600 (2022).
4. Hu GW, Ma WL, Hu DB et al. Real-space nanoimaging of hyperbolic shear polaritons in a monoclinic crystal. *Nat Nanotechnol* **18**, 64–70 (2023).
5. Ma WL, Hu GW, Hu DB et al. Ghost hyperbolic surface polaritons in bulk anisotropic crystals. *Nature* **596**, 362–366 (2021).
6. Shahzadi M, Zheng CY, Ahmad S et al. Exciton-polariton based WS_2 polarization modulator controlled by optical Stark beam. *Opto-Electron Adv* **5**, 200066 (2022).
7. Dai S, Fei Z, Ma Q et al. Tunable phonon polaritons in atomically thin van der Waals crystals of boron nitride. *Science* **343**, 1125–1129 (2014).
8. Basov DN, Fogler MM, García de Abajo FJ. Polaritons in van der Waals materials. *Science* **354**, aag1992 (2016).
9. Ma WL, Alonso-González P, Li SJ et al. In-plane anisotropic and ultra-low-loss polaritons in a natural van der Waals crystal. *Nature* **562**, 557–562 (2018).
10. Caldwell JD, Aharonovich I, Cassabois G et al. Photonics with hexagonal boron nitride. *Nat Rev Mater* **4**, 552–567 (2019).
11. Taboada-Gutiérrez J, Álvarez-Pérez G, Duan JH et al. Broad spectral tuning of ultra-low-loss polaritons in a van der Waals crystal by intercalation. *Nat Mater* **19**, 964–968 (2020).
12. Wu YJ, Duan JH, Ma WL et al. Manipulating polaritons at the extreme scale in van der Waals materials. *Nat Rev Phys* **4**, 578–594 (2022).
13. Poddubny A, Iorsh I, Belov P et al. Hyperbolic metamaterials. *Nat Photon* **7**, 948–957 (2013).
14. Zhang Q, Hu GW, Ma WL et al. Interface nano-optics with van der Waals polaritons. *Nature* **597**, 187–195 (2021).
15. Li PN, Lewin M, Kretinin AV et al. Hyperbolic phonon-polaritons in boron nitride for near-field optical imaging and focusing. *Nat Commun* **6**, 7507 (2015).
16. Dai S, Ma Q, Andersen T et al. Subdiffractional focusing and guiding of polaritonic rays in a natural hyperbolic material. *Nat Commun* **6**, 6963 (2015).
17. Li Y, Li W, Han TC et al. Transforming heat transfer with thermal metamaterials and devices. *Nat Rev Mater* **6**, 488–507 (2021).
18. Gomez-Diaz JS, Alù A. Flatland optics with hyperbolic metasurfaces. *ACS Photonics* **3**, 2211–2224 (2016).
19. Correas-Serrano D, Alù A, Gomez-Diaz JS. Plasmon canalization and tunneling over anisotropic metasurfaces. *Phys Rev B* **96**, 075436 (2017).
20. Li PN, Hu GW, Dolado I et al. Collective near-field coupling and nonlocal phenomena in infrared-phononic metasurfaces for nano-light canalization. *Nat Commun* **11**, 3663 (2020).
21. Zhang Q, Zhen Z, Yang YF et al. Negative refraction inspired polariton lens in van der Waals lateral heterojunctions. *Appl Phys Lett* **114**, 221101 (2019).
22. Lin X, Yang Y, Rivera N et al. All-angle negative refraction of highly squeezed plasmon and phonon polaritons in graphene–boron nitride heterostructures. *Proc Natl Acad Sci USA* **114**, 6717–6721 (2017).
23. Kumar A, Low T, Fung KH et al. Tunable light–matter interaction and the role of hyperbolicity in graphene-hBN system. *Nano Lett* **15**, 3172–3180 (2015).
24. Bapat A, Dixit S, Gupta Y et al. Gate tunable light–matter interaction in natural biaxial hyperbolic van der Waals heterostructures. *Nanophotonics* **11**, 2329–2340 (2022).
25. Dai S, Ma Q, Liu MK et al. Graphene on hexagonal boron nitride as a tunable hyperbolic metamaterial. *Nat Nanotechnol* **10**, 682–686 (2015).
26. Brar VW, Jang MS, Sherrott M et al. Hybrid surface-phonon-plasmon polariton modes in graphene/monolayer h-BN heterostructures. *Nano Lett* **14**, 3876–3880 (2014).
27. Zeng YL, Ou QD, Liu L et al. Tailoring topological transitions of anisotropic polaritons by interface engineering in biaxial crystals. *Nano Lett* **22**, 4260–4268 (2022).
28. Hu GW, Krasnok A, Mazor Y et al. Moiré hyperbolic metasurfaces. *Nano Lett* **20**, 3217–3224 (2020).
29. Hu GW, Ou QD, Si GY et al. Topological polaritons and photonic magic angles in twisted α-MoO_3 bilayers. *Nature* **582**, 209–213 (2020).
30. Chen MY, Lin X, Dinh TH et al. Configurable phonon polaritons in twisted α-MoO_3. *Nat Mater* **19**, 1307–1311 (2020).
31. Zhang Q, Ou QD, Hu GW et al. Hybridized hyperbolic surface phonon polaritons at α-MoO_3 and polar dielectric interfaces. *Nano Lett* **21**, 3112–3119 (2021).
32. Zheng ZB, Sun FS, Huang WC et al. Phonon polaritons in twisted double-layers of hyperbolic van der Waals crystals. *Nano Lett* **20**, 5301–5308 (2020).
33. Wang C, Xie YG, Ma JW et al. Twist-angle and thickness-ratio tuning of plasmon polaritons in twisted bilayer van der Waals films. *Nano Lett* **23**, 6907–6913 (2023).
34. Álvarez-Pérez G, González-Morán A, Capote-Robayna N et al. Active tuning of highly anisotropic phonon polaritons in van der Waals crystal slabs by gated graphene. *ACS Photon* **9**, 383–390 (2022).
35. Hu H, Chen N, Teng HC et al. Doping-driven topological polaritons in graphene/α-MoO_3 heterostructures. *Nat Nanotechnol* **17**, 940–946 (2022).
36. Hu H, Chen N, Teng HC et al. Gate-tunable negative refraction of mid-infrared polaritons. *Science* **379**, 558–561 (2023).
37. Yu SJ, Yao HL, Hu GW et al. Hyperbolic Polaritonic Rulers Based on van der Waals α-MoO3 Waveguides and Resonators. *ACS Nano* **17**, 23057–23064 (2023).
38. Fali A, White ST, Folland TG et al. Refractive index-based control of hyperbolic phonon-polariton propagation. *Nano Lett* **19**, 7725–7734 (2019).
39. Wehmeier L, Yu SJ, Chen XZ et al. Tunable Phonon Polariton Hybridization in a van der Waals Hetero‐Bicrystal. *Adv Mater* , 2401349 (2024).
40. Duan J, Álvarez-Pérez G, Voronin KV et al. Enabling propagation of anisotropic polaritons along forbidden directions via a topological transition. *Sci Adv* **7**, eabf2690 (2021).
41. Hong PL, Xu L, Rahmani M. Dual bound states in the continuum enhanced second harmonic generation with transition metal dichalcogenides monolayer. *Opto-Electron Adv* **5**, 200097 (2022).
42. Yan SQ, Zuo Y, Xiao SS et al. Graphene photodetector employing double slot structure with enhanced responsivity and large bandwidth. *Opto-Electron Adv* **5**, 210159 (2022).
43. Zhang WL, Çakıroğlu O, Al-Enizi A et al. Solvent-free fabrication of broadband WS_2 photodetectors on paper. *Opto-Electron Adv* **6**, 220101 (2023).
44. Lee IH, He MZ, Zhang X et al. Image polaritons in boron nitride for extreme polariton confinement with low losses. *Nat Commun* **11**, 3649 (2020).

45. Menabde SG, Heiden JT, Cox JD et al. Image polaritons in van der Waals crystals. *Nanophotonics* **11**, 2433–2452 (2022).
46. Zheng ZB, Xu NS, Oscurato SL et al. A mid-infrared biaxial hyperbolic van der Waals crystal. *Sci Adv* **5**, eaav8690 (2019).
47. Álvarez-Pérez G, Voronin KV, Volkov VS et al. Analytical approximations for the dispersion of electromagnetic modes in slabs of biaxial crystals. *Phys Rev B* **100**, 235408 (2019).
48. Högström H, Valizadeh S, Ribbing CG. Optical excitation of surface phonon polaritons in silicon carbide by a hole array fabricated by a focused ion beam. *Opt Mater* **30**, 328–333 (2007).
49. Gubbin CR, Martini F, Politi A et al. Strong and coherent coupling between localized and propagating phonon polaritons. *Phys Rev Lett* **116**, 246402 (2016).
50. Sehmi HS, Langbein W, Muljarov EA. Optimizing the Drude-Lorentz model for material permittivity: Method, program, and examples for gold, silver, and copper. *Phys Rev B* **95**, 115444 (2017).
51. Ambrosio A, Tamagnone M, Chaudhary K et al. Selective excitation and imaging of ultraslow phonon polaritons in thin hexagonal boron nitride crystals. *Light Sci Appl* **7**, 27 (2018).
52. Caldwell JD, Kretinin AV, Chen YG et al. Sub-diffractional volume-confined polaritons in the natural hyperbolic material hexagonal boron nitride. *Nat Commun* **5**, 5221 (2014).
53. Dai SY, Tymchenko M, Yang YF et al. Manipulation and steering of hyperbolic surface polaritons in hexagonal boron nitride. *Adv Mater* **30**, 1706358 (2018).
54. Narimanov EE. Dyakonov waves in biaxial anisotropic crystals. *Phys Rev A* **98** 013818 (2018).
55. Zhang ZM. *Nano/Microscale Heat Transfer* (Springer, Cham, 2020).
56. Polder D, Van Hove M. Theory of radiative heat transfer between closely spaced bodies. *Phys Rev B* **4**, 3303 (1971).
57. St-Gelais R, Guha B, Zhu LX et al. Demonstration of strong near-field radiative heat transfer between integrated nanostructures. *Nano Lett* **14**, 6971–6975 (2014).
58. Kim K, Song B, Fernández-Hurtado V et al. Radiative heat transfer in the extreme near field. *Nature* **528**, 387–391 (2015).
59. Messina R, Antezza M, Ben-Abdallah P. Three-body amplification of photon heat tunneling. *Phys Rev Lett* **109**, 244302 (2012).
60. Fernández-Hurtado V, García-Vidal FJ, Fan SH et al. Enhancing near-field radiative heat transfer with Si-based metasurfaces. *Phys Rev Lett* **118**, 203901 (2017).
61. Rytov SM. *Theory of Electric Fluctuations and Thermal Radiation* (Air Force Cambridge Research Center, Bedford, 1953).
62. De Wilde Y, Formanek F, Carminati R et al. Thermal radiation scanning tunnelling microscopy. *Nature* **444**, 740–743 (2006).
63. Challener WA, Peng CB, Itagi AV et al. Heat-assisted magnetic recording by a near-field transducer with efficient optical energy transfer. *Nat Photon* **3**, 220–224 (2009).
64. Elzouka M, Ndao S. Near-field NanoThermoMechanical memory. *Appl Phys Lett* **105**, 243510 (2014).
65. Zhao B, Zhang ZM. Enhanced photon tunneling by surface plasmon–phonon polaritons in Graphene/hBN heterostructures. *J Heat Transfer* **139** 022701 (2017).
66. Wu XH, Fu CJ, Zhang ZM. Influence of hBN orientation on the near-field radiative heat transfer between graphene/hBN heterostructures. *J Photon Energy* **9**, 032702 (2019).
67. Joulain K, Mulet JP, Marquier F et al. Surface electromagnetic waves thermally excited: radiative heat transfer, coherence properties and Casimir forces revisited in the near field. *Surf Sci Rep* **57**, 59–112 (2005).
68. Fu CJ, Zhang ZM. Nanoscale radiation heat transfer for silicon at different doping levels. *Int J Heat Mass Tran* **49**, 1703–1718 (2006).
69. Mittapally R, Lim JW, Meyhofer E et al. Quantifying the effect of nanofilms on near-field radiative heat transfer. *ACS Photon* **10**, 2474–2480 (2023).
70. Su CS, Fu CJ. Near-field radiative heat transfer between two α-quartz plates having hyperbolic and double-negative-permittivity bands. *Int J Heat Mass Tran* **196**, 123235 (2022).
71. Liu XL, Zhang RZ, Zhang ZM. Near-field radiative heat transfer with doped-silicon nanostructured metamaterials. *Int J Heat Mass Tran* **73**, 389–398 (2014).
72. Basu S, Zhang ZM. Ultrasmall penetration depth in nanoscale thermal radiation. *Appl Phys Lett* **95** 133104 (2009).

Acknowledgements

This work was supported by the National Natural Science Foundation of China (Nos. 52106099 and 51576004), the Natural Science Foundation of Shandong Province (No. ZR2022YQ57), and the Taishan Scholars Program.

Author contributions

All the authors were involved in designing the research, performing the research and writing the paper.

Competing interests

The authors declare no competing financial interests.

Supplementary information

Supplementary information for this paper is available at https://doi.org/10.29026/oes.2024.240002

Scan for Article PDF